

THESIS FOR THE DEGREE OF DOCTOR OF PHILOSOPHY

Assessment of cavitation erosion risk based on  
single-fluid simulation of cavitating flows

MOHAMMAD HOSSEIN ARABNEJAD



Department of Mechanics and Maritime Sciences  
CHALMERS UNIVERSITY OF TECHNOLOGY  
Göteborg, Sweden 2020

Assessment of cavitation erosion risk based on single-fluid simulation of  
cavitating flows

MOHAMMAD HOSSEIN ARABNEJAD  
ISBN: 978-91-7905-363-5

© MOHAMMAD HOSSEIN ARABNEJAD, 2020

Series number: 4830  
ISSN 0346-718X

Department of Mechanics and Maritime Sciences  
Chalmers University of Technology  
SE-412 96 Göteborg  
Sweden  
Telephone + 46 (0)31-772 1000

Printed by Chalmers Reproservice  
Göteborg, Sweden 2020

---

## **Assessment of cavitation erosion risk based on single-fluid simulation of cavitating flows**

MOHAMMAD HOSSEIN ARABNEJAD, 2020

Department of Mechanics and Maritime Sciences, Chalmers University of Technology

### **Abstract**

Cavitation erosion is material loss due to the repetitive collapse of cavities near the surface. This phenomenon is one of the limiting factors in the design of high-performance marine propulsors as it restricts their reliability and increases their operational cost. To avoid such consequences, erosion assessment using experimental methods are traditionally performed in the design process of marine propulsors. These methods are, however, expensive and can be applied only in model-scale at a late stage of the design. Alternative to these are numerical assessment methods which can be applied both in model-scale and full-scale at any stage of the design. Development and application of such numerical methods are the main objectives of this thesis.

Two numerical erosion assessment methods are included in this thesis and both are based on single-fluid simulation of cavitating flows. The first method which is developed in this thesis, can assess the risk of cavitation erosion based on incompressible simulations of cavitating flows. This method which considers an energy transfer between collapsing cavities and eroded surface, offers two advantages over other published methods. First, the method takes into account both shock-waves and micro-jets as the mechanisms for cavitation erosion, while previous published methods have considered only one of these erosion mechanisms. Secondly, the method estimates the risk of cavitation erosion based on the collapse induced kinetic energy in the surrounding liquid instead of the potential energy of collapsing cavities, which avoids the uncertainty regarding the calculation of the collapse driving pressure in the potential energy equation. The second numerical assessment method is based on compressible simulation of cavitating flows which has been developed by Schnerr et al. [1] and Mihatsch et al. [2]. This method captures the collapse-induced shock-waves and uses the strength and the frequency of these shock-waves to identify the erosion-sensitive areas. These numerical assessment methods are implemented in the OpenFOAM framework and the implementation has been validated against analytical solutions and an experimental study.

Using the above mentioned numerical assessment methods, three types of cavitating flows are investigated. These are 3D leading edge cavitation over a wing, a cavitating flow in an axisymmetric nozzle, and cavitating flows in water-jet pumps. For the leading edge cavitation, the numerical methods are combined with experimental techniques in order to investigate the relation between the shedding

---

mechanisms of transient cavities and aggressive collapse events. This investigation shows that the leading-edge cavitation leads to the shedding of small and large-scale cavitating structures, both of which are associated with high risk of cavitation erosion. The small-scale cavitating structures are, however, shown to possess a higher risk of cavitation erosion, as they result in a large number of aggressive collapse events which are close to the surface. The second studied case is the cavitating flow in an axisymmetric nozzle which is simulated with the objective of validating the numerical erosion assessment methods included in this thesis. The risk of cavitation erosion predicted by these methods is compared with the experimental erosion investigation by Franc et al. [3] and this comparison shows both methods are capable of identifying areas with high erosion risk. Furthermore, using the numerical results, the hydrodynamic mechanism responsible for the high risk of cavitation erosion at the inception region of the sheet cavity is investigated in detail. This investigation indicates that the high erosion risk in this region is closely tied to the separation of the flow entering the nozzle. The third type of studied flow is the cavitating flow in water-jet pumps. These cavitating flows are numerically investigated with two specific objectives, 1) to identify the mesh resolution requirement for high quality simulation of water-jet pumps, 2) to perform numerical erosion assessment on water jet pumps. For the first objective, the AxWJ-2 pump from Johns Hopkins University is simulated using different mesh resolutions and the results are compared with available experimental data in the literature. For the second objective, the cavitating flows in a commercial water-jet pump are investigated. The investigation includes applying the developed incompressible erosion assessment method to two flow conditions with different risk of cavitation erosion. The results of these numerical erosion assessment are compared with the experimental paint tests performed at Kongsberg Hydrodynamic Research Centre (KHRC). This comparison shows that the developed numerical erosion assessment method is not only able to distinguish between the conditions with different level of cavitation erosion risk but also capable of identifying the regions of high erosion risk in the most erosive flow condition. Furthermore, the hydrodynamic mechanisms leading to different risk of cavitation erosion in the two studied conditions are investigated using numerical simulation results. It is shown that this difference is due to a different distribution of axial velocity in the flow entering the pump in the two studied conditions.

**Keywords:** Cavitation, risk of cavitation erosion, water-jet pump, compressible simulation of cavitating flows, leading edge cavitation, OpenFOAM.

---

To my parents and my sister



---

## ACKNOWLEDGEMENT

This PhD thesis is the output of the effort and support of several people to whom I am extremely grateful. First and foremost, I would like to express my sincere gratitude to my supervisor, Prof. Rickard E. Bensow, for the continuous support of my Ph.D. study and related research, for his patience, motivation, and immense knowledge. His guidance helped me in all the time of research and writing of this thesis. I could not have imagined having a better supervisor like him.

Many thanks to my co-supervisor in the last two years of my Ph.D., Dr. Urban Svennberg, for giving his valuable comments and suggestions for our manuscripts, and also for sharing his industrial experience which helped me understand the big picture of my research.

I am also profoundly grateful for the substantial contributions of the co-authors of the papers appended to this thesis. Thank you, Dr. Ali Amini, Dr. Arash Eslamdoost, and Dr. Mohamed Farhat. I am delighted to have worked with you and I look forward to working with you again.

I would like to thank Prof. Jonas Ringsberg, the head of Marine Technology division, for his support and for providing a perfect working environment. Special thanks also goes to my colleagues in Marine Technology division for the discussions we had during lunches and coffee breaks. It has been a pleasure to work with all of you.

Financial support for this work has been provided by the EU H2020 project CaFE, a Marie Skłodowska-Curie Action Innovative Training Network project, grant number 642536, and Kongsberg Maritime through the University Technology Centre in Computational Hydrodynamics hosted at the Division of Marine Technology, Department of Mechanics and Maritime Sciences at Chalmers. The simulations were performed on resources at Chalmers Centre for Computational Science and Engineering (C3SE) as well as National Supercomputer Center at Linköping University (NSC) provided by the Swedish National Infrastructure for Computing (SNIC).

Last but not the least, I would like to thank my family: my deceased father to whom I owe so much and my mother and sister who support me unconditionally through my Ph.D.





---

## LIST OF PAPERS

The thesis consists of an introduction and the following publications:

- Paper A** M.H. Arabnejad, A. Amini, M. Farhat, and R.E. Bensow. Numerical and experimental investigation of shedding mechanisms from leading-edge cavitation. *International Journal of Multiphase Flow*, 119, 123-143, 2019.
- Contribution:* *The author of this thesis contributed in the planning and writing of the paper, performed the simulations and post-processing of the numerical results, participated in the planning and performing the experimental part, and performed the post-processing of the experimental results.*
- Paper B** M.H. Arabnejad, A. Amini, M. Farhat, and R.E. Bensow. Hydrodynamic mechanisms of aggressive collapse events in leading edge cavitation. *Journal of Hydrodynamics*, 32, 6–19 (2020).
- Contribution:* *The author of this thesis contributed in the planning and writing of the paper, performed the simulations and post-processing of the numerical results, participated in the planning and performing the experimental part, and performed the post-processing of the experimental results.*
- Paper C** M.H. Arabnejad, U. Svennberg, and R.E. Bensow. Numerical assessment of cavitation erosion risk using incompressible simulation of cavitating flows, Manuscript (Revision submitted to *Wear*).
- Contribution:* *The author of this thesis contributed in the planning and writing of the paper, developed the method for assessing the risk of cavitation erosion, and performed the simulations and post-processing of the numerical results.*
- Paper D** M.H. Arabnejad, A. Eslamdoost, U. Svennberg, and R.E. Bensow. Scale resolving simulations of the non-cavitating and cavitating flows in an axial water jet pump, to be presented at 33rd Symposium on Naval Hydrodynamics, Osaka Japan.
- Contribution:* *The author of this thesis contributed in the planning and writing of the paper and performed the simulations and post-processing of the numerical results.*

---

**Paper E** M.H. Arabnejad, U. Svennberg, and R.E. Bensow. Numerical assessment of cavitation erosion in a commercial water-jet pump (Manuscript)

*Contribution:* *The author of this thesis contributed in the planning and writing of the paper and performed the simulations and post-processing of the numerical results.*

## OTHER RELEVANT PUBLICATIONS

In addition to the appended papers, I have been the first author of the following publications:

- Paper I** M.H. Arabnejad , R.E. Bensow, and C. Eskilsson, Density-based Compressible Solver with Equilibrium Cavitation Model in OpenFOAM, 19th Numerical Towing Tank Symposium, St. Pierre d'Oleron, France, 2017.
- Paper II** M. H. Arabnejad ,and R. Bensow, A methodology to identify erosive collapse events in incompressible simulation of cavitating flows, 20th Numerical Towing Tank Symposium, Wageningen, Netherland, 2017.
- Paper III** M.H. Arabnejad, A. Amini, R.E. Bensow, and M. Farhat. Experimental and numerical investigation of the cavitating flows over a modified NACA0009 foil. In The 10th International Symposium on Cavitation (CAV2018), Baltimore, Maryland, USA, 2018.
- Paper IV** M.H. Arabnejad. Numerical and Experimental Investigation of Hydrodynamic Mechanisms in Erosive Sheet Cavitation. Technical report, Department of Mechanics and Maritime Sciences, Chalmers University of Technology, 2018. Lic.Eng. Thesis, Report no 2018:19.
- Paper V** M.H. Arabnejad, A. Eslamdoost, U. Svennberg, and R.E. Bensow, Effect of Cavitation on the Structure of Tip Leakage Vortex in an Axial Water-Jet Pump, 22nd Numerical Towing Tank Symposium, Tomar, Portugal, 2019.
- Paper VI** M.H. Arabnejad, R.E. Bensow, dbnsCavitatingFoam: A density-based solver with equilibrium cavitation models in OpenFOAM framework, unpublished work (available in preprint).

---

# ***CONTENTS***

---

<b>1</b>	<b>Introduction</b>	<b>1</b>
1.1	Leading-edge cavitation . . . . .	1
1.2	Vortex cavitation . . . . .	2
1.3	Cavitation erosion . . . . .	3
1.4	Numerical assessment of cavitation erosion . . . . .	3
1.5	Objectives and scope of this thesis . . . . .	5
1.6	Thesis outline . . . . .	6
<b>2</b>	<b>Numerical methods</b>	<b>7</b>
2.1	Governing equations of cavitating flows . . . . .	7
2.1.1	Volume filtering . . . . .	8
2.1.2	ILES approach . . . . .	9
2.1.3	WALE approach . . . . .	9
2.2	Cavitation modeling . . . . .	10
2.2.1	Transport equation based cavitation model . . . . .	10
2.2.2	Barotropic cavitation model . . . . .	11
2.3	Numerical erosion assessment . . . . .	12
2.3.1	Method based on compressible simulation . . . . .	12
2.3.2	Method based on incompressible simulation . . . . .	13
<b>3</b>	<b>Studied cases</b>	<b>19</b>
3.1	NACA0009 foil . . . . .	19
3.1.1	Experimental set-up . . . . .	19
3.1.2	Computational domain . . . . .	21
3.2	Axisymmetric cavitating nozzle flow . . . . .	23
3.3	Water-jet pumps . . . . .	23
3.3.1	AxWJ-2 water-jet pump . . . . .	24
3.3.2	Kongsberg water-jet pump . . . . .	26

<b>4</b>	<b>Summary of appended papers</b>	<b>29</b>
4.1	Paper A . . . . .	29
4.2	Paper B . . . . .	32
4.3	Paper C . . . . .	35
4.4	Paper D . . . . .	37
4.5	Paper E . . . . .	39
<b>5</b>	<b>Concluding remarks</b>	<b>43</b>
	<b>REFERENCES</b>	<b>45</b>
<b>A</b>	<b>Appended Papers A-E</b>	<b>51</b>

---

# 1

## *Introduction*

---

Despite numerous research, cavitation and its detrimental effects are still one of the biggest challenges in the design of highly efficient marine propulsors. Hydrodynamic cavitation in these machines occurs when vapor structures are generated in the liquid flow due to a pressure drop. These cavities are often transported by the flow to high pressure regions where they can collapse violently. These violent collapses can induce high mechanical loads in nearby surfaces leading to erosion and vibration and also increase the level of noise which has been proven to be harmful for marine life. In marine propulsors, different types of cavitation can be seen depending on the reason for the pressure drop leading to cavitation. The most common types are leading-edge cavitation and vortex cavitation near the tip of the rotating blades.

### **1.1 LEADING-EDGE CAVITATION**

Leading-edge cavitation is a cavity in the form of a sheet which is attached to the blade. This sheet cavity forms when the flow acceleration, caused by the curvature of streamlines around the blade, leads to a region of low pressure. If the pressure in this region drops below vapor pressure, an attached cavity can form. Previous numerical and experimental studies have shown that instabilities in the leading-edge cavitation can lead to shedding of cloud cavities. Two main mechanisms responsible for these instabilities are the re-entrant jet [4, 5] and the shock-wave [6, 7]. The re-entrant jet is an upstream moving liquid flow underneath the sheet cavity. This jet is created when some portion of the flow above the interface of the cavity is redirected upstream due to a pressure gradient at the closure line. The re-entrant flow can lead to two types of shedding, large-scale shedding and small-scale shedding. These types of shedding are shown in Figure 1.1. The large-scale shedding is mostly periodic with the frequency governed by a universal Strouhal law while the small-scale shedding is often irregular and does not have any domi-

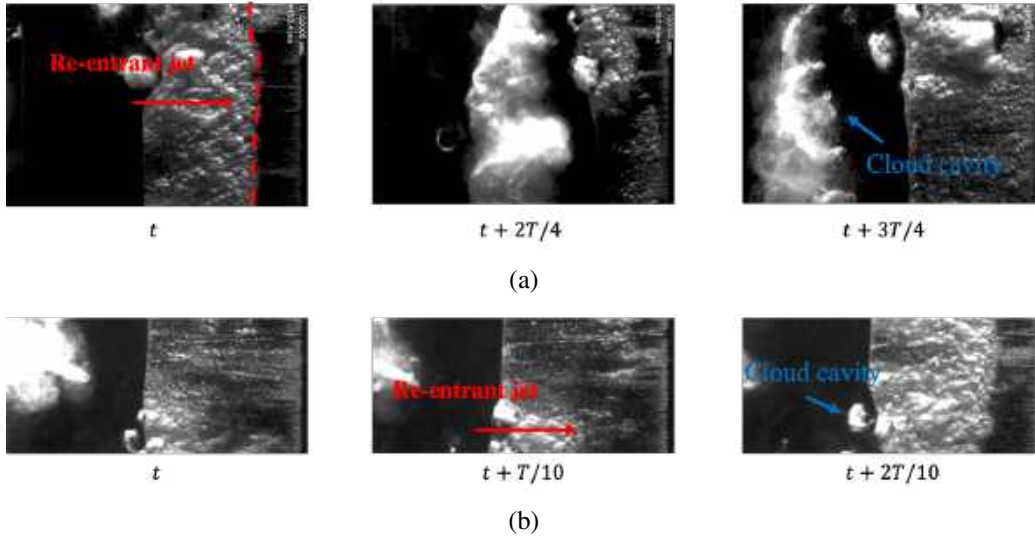


**Figure 1.1:** Shedding mechanisms due to re-entrant jet in the leading-edge cavitation over a foil, a) Large-scale shedding, b) Small-scale shedding.

nant frequency. The second mechanism of shedding from leading edge cavitation is the condensation shock wave. The formation of this shock-wave was firstly suggested by Jakobsen [8]. However, Ganesh et al. [7] has recently observed and investigated the formation of this shock-wave using X-ray densitometry and high-speed visualization. Using the instantaneous void-fraction field obtained by X-ray densitometry, these authors showed that when the shock-wave moves upstream, a large scale cloud cavity is pinched off from the attached cavity.

## 1.2 VORTEX CAVITATION

Another type of cavitation in marine propulsors is vortex cavitation. This type of cavitation can be seen mostly in the tip region of a rotating blade. In water-jet pumps, this type of cavitation occur due to the formation of Tip Leakage Vortex (TLV). The formation of this vortex is schematically shown in Figure 1.2. In the tip region, the pressure difference between the suction side and the pressure side of the blade leads to a leakage flow in the gap between the impeller blade and the casing. The interaction between this leakage flow and the flow in the passage results in the formation of vortical structures which are detached from the impeller blade tip [9]. As these detached vortices travel further in the passage, they wrap around each other and form the main core of TLV [10]. In certain inflow condition, the pressure around the core of TLV can drop below vapor pressure which in turn leads to the formation of cavitation [11]. Previous experimental studies [12, 13] have shown that the formation of TLVs and their resultant cavitating structures results in a high level of noise and performance degradation. According to Tan et al. [14], this performance degradation occurs when the interaction between the leading edge cavitation and TLV cavitation leads to the formation of Perpendicular

Cavitating Vortices (PCVs). As these vortices travel deep in the passage, they decrease the blade loading leading to the onset of cavitation breakdown.

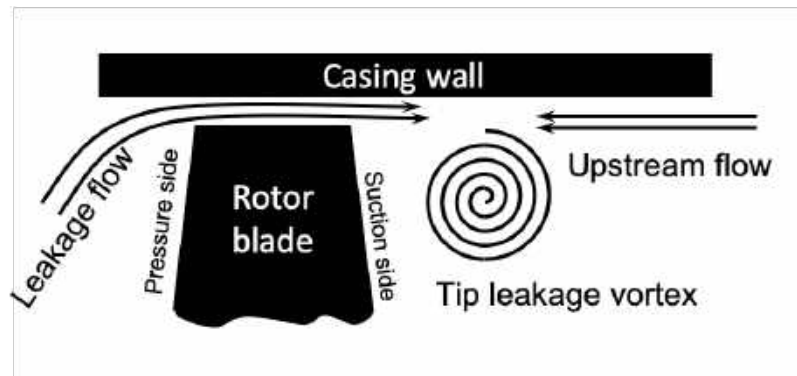


**Figure 1.2:** Formation of Tip leakage vortex.

### 1.3 CAVITATION EROSION

Both leading-edge and vortex cavitation can create transient cavities which can collapse violently as they are transported to high pressure regions. If these collapses occur relatively near a surface, they induce high mechanical loads and stress levels on the surface which can lead to cavitation erosion. Two mechanisms of cavitation erosion, shock-waves and micro-jets, are responsible for this high level of stress. The formation of the collapse-induced shock-waves, shown in Figure 1.3b, has been observed in the numerical simulations, experimental investigation and analytical analyses of the spherical collapse of a bubble [15, 16]. This shock-wave is created when the converging flow toward the centre of the collapse in the surrounding liquid stops at the end of collapse. This sudden change in the velocity of surrounding liquid leads to a local pressure increase which propagates in the surrounding liquid in the form of shock-waves. When these shock-waves hit the surface, they increase the pressure on the surface which induce a high mechanical load. Another mechanism responsible for cavitation erosion is a jet-like flow called a micro-jet. As shown in Figure 1.3c, the micro-jet forms when a bubble collapses near the surface. When this micro-jet impinges the nearby surface, it generates a water-hammer like pressure which can remove material from the surface in certain circumstances.

### 1.4 NUMERICAL ASSESSMENT OF CAVITATION EROSION

As cavitation erosion restricts the durability and the operating life-time of marine propulsion systems, the design procedure of these systems often includes a stage where the risk of cavitation erosion is assessed. This assessment is mostly done through experimental methods such as high-speed videos [19] complemented by

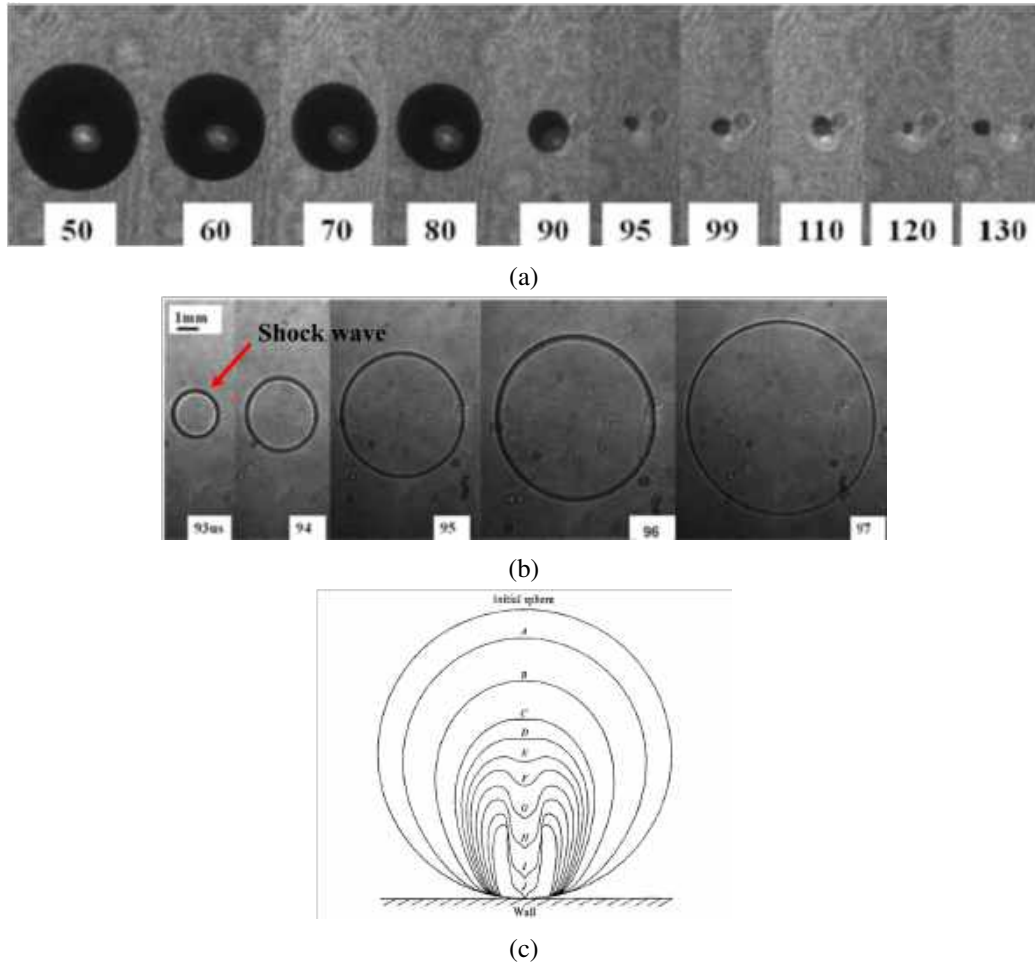


**Figure 1.3:** Two mechanisms of cavitation erosion, a and b) formation of shock-waves after the collapse of a spherical bubble [17], c) the formation of micro-jet for a collapsing bubble near the surface [18].

paint test and/or acoustic measurements [20, 21, 22]. Although such experimental methods are common, they suffer from two limitations. Firstly, these methods can be applied only for the model scale device and the risk of cavitation in full-scale needs to be estimated based on experience or ad-hoc correlation. Secondly, the experimental methods can provide erosion assessment only at a late-stage of the design where any modification in the design due to assessed high risk can be expensive.

To address the above mentioned limitations of experimental erosion assessment, numerical methods capable of performing this assessment are highly desired. Several such numerical methods have been proposed in the literature. These methods can be classified into two categories based on whether they consider the liquid to be compressible or not. In the first category where the liquid compressibility is considered, the collapse induced shock-wave can be captured in the simulation. As these shock-waves are one mechanism of cavitation erosion,



the strength of these shock-waves can be used for erosion assessment. Several studies have successfully applied this type of numerical erosion assessment methods to the viscous simulation of high-speed cavitating flows in diesel injectors [23, 24, 25]. However, for low-speed cavitating flows in marine propulsors, these compressible methods can only be applied in inviscid simulations with high computational cost [26, 27].

The second category of numerical erosion assessment methods are based on incompressible simulation of cavitating flows. In contrast to compressible methods, these methods have relatively reasonable computational cost for low-speed cavitating flows and can be applied to viscous simulations of marine propulsors. Several of such incompressible methods have been proposed in the literature [28, 29, 30, 31]. Van et al. [32] reviewed several of these incompressible erosion assessment methods and concluded that methods based on energy description of cavitation erosion [33, 29, 19] are more suitable for numerical erosion assessment. This energy description considers a balance between cavitation erosion and the potential energy of collapsing vapor structures, which is assumed to be proportional to the vapor content of collapsing cavity structures and the collapse driving pressure. Although a few of such energy-based erosion assessment methodologies have been proposed [29, 34] and applied [35, 36] in the literature, they all suffer from uncertainty regarding the calculation of the collapse driving pressure in the definition of potential energy according to Schenke et al. [34]; therefore further research is necessary to develop reliable energy-based methods for assessing cavitation erosion risk.

## **1.5 OBJECTIVES AND SCOPE OF THIS THESIS**

Previous numerical studies by Huuva [37], Lu et al. [38], Asnaghi and Bensow [39] have shown that current numerical simulation of cavitating flows are able to reproduce the large-scale cavity dynamics controlling cavitation erosion. Building on these capabilities, this thesis is focused on the application of such numerical simulations in the assessment of cavitation erosion risk with the following objectives:

1. Develop and implement a numerical method capable of assessing the risk of cavitation erosion.
2. Investigate hydrodynamic mechanisms leading to aggressive collapse events
3. Apply numerical assessment of cavitation erosion risk in industrial applications.

To achieve the first objective, two numerical erosion assessment methods are considered in this thesis. The first one is the numerical method which predicts the risk of cavitation erosion based on the energy description of cavitation erosion [33]. This method is originally developed in this thesis. The second numerical

assessment method, which is developed by Mihatsch et al. [2] and Schnerr et al. [1], is based on the compressible simulation of cavitating flows. Both of these numerical methods are implemented in the OpenFOAM framework and they are validated against the experimental studies available in the literature as well as the ones presented in this paper.

For the second objective, the leading-edge cavitation over a 3D wing is investigated using numerical and experimental methods. These methods are first employed to identify the large-scale and small-scale shedding mechanisms of transient cavities in the leading-edge cavitation. The relation between these shedding mechanisms and the areas with high risk of cavitation erosion is then investigated using the implemented compressible erosion assessment method and the experimental techniques.

For the last objective, the developed numerical erosion assessment method for incompressible simulations is applied to a commercial water-jet pump. As a high quality simulation of cavitating flows is a prerequisite of any numerical erosion assessment, the first task in this part is devoted to identifying the mesh resolution requirement for high quality simulations in water-jet pumps. The non-cavitating and cavitating flows in the AxWJ-2 water-jet pump [40] are simulated using different mesh resolutions and the results are compared with experimental results of Li et al. [41] and Tan et al. [14]. Using the identified mesh requirement in the first task, the simulation of a commercial water-jet pump is performed and the risk of cavitation erosion is assessed numerically. The numerical erosion assessment is performed for two cavitating conditions which have been identified to have different risk of cavitation erosion according to the experimental paint test. Using the information provided by the numerical erosion assessment, the reasons behind a different risk of cavitation erosion for the two studied conditions are investigated.

### 1.6 THESIS OUTLINE

This thesis is structured in five chapters and an appendix. Following this introduction chapter, the next chapter describes the numerical methods used in this thesis. This description includes the governing equations for cavitating flows, the cavitation modelling used in the present thesis, as well as the developed and implemented numerical erosion assessment methods. Chapter 3 is devoted to the description of studied cases including their flow configurations, the description of their computational meshes, and studied flow conditions. In Chapter 4, the objective and summary of findings for each appended paper are presented. Chapter 5 includes the conclusion of studies performed in the thesis, and the prepared/published journal and conference papers are included in the appendix.

---

# 2

## *Numerical methods*

---

In this chapter, the numerical methods used in this thesis are explained in three sections. The first section presents the governing equations for cavitating flows, the volume filtering of governing equations and the modeling of sub-grid scale terms in filtered equations. The second section describes the cavitation modeling used in the thesis and the last section is devoted to the description of numerical erosion assessment methods.

### 2.1 GOVERNING EQUATIONS OF CAVITATING FLOWS

In cavitating flows, two phases can co-exist, liquid ( $k = l$ ) and vapor ( $k = v$ ). If one assumes that the effect of surface tension and gravity are negligible and the flow is isothermal, the governing equations in terms of phase-weighted variables can be written as,

$$\frac{\partial}{\partial t}(\chi^k \rho^k) + \nabla \cdot (\chi^k \rho^k \mathbf{u}^k) = \dot{m}^k \delta_i, \quad (2.1)$$

$$\frac{\partial}{\partial t}(\chi^k \rho^k \mathbf{u}^k) + \nabla \cdot (\chi^k \rho^k \mathbf{u}^k \otimes \mathbf{u}^k) + \nabla \cdot (\chi^k [p^k \mathbf{I} - \boldsymbol{\tau}^k]) = \mathbf{S}_m^k \delta_i, \quad (2.2)$$

where  $\rho^k$ ,  $\mathbf{u}^k$ , and  $p^k$  are, respectively, the density, the velocity vector, and the pressure of the phase  $k$ . Further,  $\dot{m}_i$  and  $\mathbf{S}_m^k$ , are, respectively, the mass and momentum transfer terms at the interface,  $\mathbf{I}$  is the identity tensor,  $\boldsymbol{\tau}^k$  is the viscous stress tensor,  $\delta_i$  is the Dirac function defined on the interface, and  $\mathbf{n}^k$  is the outwardly directed normal unit vector to the interface of the volume occupied by phase  $k$ . In the above equations,  $\chi^k$ , is the phase indicator which can be defined as,

$$\chi^k(\mathbf{x}, t) = \begin{cases} 1 & \mathbf{x} \in \text{phase } k \\ 0 & \mathbf{x} \notin \text{phase } k, \end{cases} \quad (2.3)$$

where  $\mathbf{x}$  is the location vector. It should be mentioned that the transfer terms on the right hand of the equations 2.1 and 2.2 satisfy the so called jump conditions. With the assumption that the surface tension is negligible, these jump conditions can be written as,

$$\begin{aligned} \sum_{k=1}^2 \dot{m}^k &= 0, \\ \sum_{k=1}^2 \mathbf{S}_m^k &= 0. \end{aligned} \quad (2.4)$$

In order to solve the above governing equations in the finite volume approach, a volume filtering should be applied on these equation. In the following, this volume filtering is presented.

### 2.1.1 Volume filtering

The volume filtering of the governing equations are achieved by averaging each variable,  $\phi^k$ , over the cell  $\Omega$  with the volume of  $V$  as

$$\hat{\phi}^k = \frac{1}{V} \int_{\Omega} \phi^k dV, \quad (2.5)$$

where  $\hat{\phi}^k$  is the volume averaged variable. This volume averaging is equivalent to the spatial filtering in LES approach using a box filter. This filtering can be written as

$$\hat{\phi}^k = \int_{-\infty}^{+\infty} G(\mathbf{x} - \xi) \phi^k(\xi, t) dt d^3 \xi. \quad (2.6)$$

where  $G$  is the mentioned box filter and  $\hat{\phi}^k$  is the filtered variable.

Using the above volume filtering and the definition of phase indicator,  $\chi^k$ , one can define the volume fraction of the phase  $k$ ,  $\alpha^k$ , as,

$$\alpha^k = \hat{\chi}^k. \quad (2.7)$$

The phasic averaged variable,  $\bar{\phi}^k$ , and Favre phasic averaged variable,  $\tilde{\phi}^k$ , can also be defined as,

$$\bar{\phi}^k = \frac{\widehat{\chi^k \phi^k}}{\alpha^k}, \quad \tilde{\phi}^k = \frac{\overline{\rho^k \phi^k}}{\bar{\rho}^k}. \quad (2.8)$$

Applying the volume filtering to the equations 2.1 and 2.2 and using the above definitions, the filtered equations can be obtained as,

$$\frac{\partial}{\partial t} (\alpha^k \bar{\rho}^k) + \nabla \cdot (\alpha^k \bar{\rho}^k \tilde{\mathbf{u}}^k) = \dot{m}, \quad (2.9)$$

$$\frac{\partial}{\partial t} (\alpha^k \bar{\rho}^k \tilde{\mathbf{u}}^k) + \nabla \cdot (\alpha^k \bar{\rho}^k \tilde{\mathbf{u}}^k \otimes \tilde{\mathbf{u}}^k) + \nabla \cdot (\alpha^k [\bar{p}^k \mathbf{I} - \bar{\boldsymbol{\tau}}^k]) + \nabla \cdot (\alpha^k \boldsymbol{\tau}_{sgs}^k) = \mathbf{S}_m, \quad (2.10)$$

where  $\dot{m}$ , and  $\mathbf{S}_m$  are, respectively, the volume filtered mass and momentum transfer terms and  $\tau_{sgs}^k = \widetilde{\bar{\rho} \mathbf{u}^k \otimes \mathbf{u}^k} - \bar{\rho}^k \tilde{\mathbf{u}}^k \otimes \tilde{\mathbf{u}}^k$  are the subgrid scale terms.

To further simplify the filtered equations, the homogeneous mixture approach can be adopted. In this approach, it is assumed that both phases share the same velocity and pressure,

$$\mathbf{u}^v = \mathbf{u}^l = \mathbf{u}, \quad p^v = p^l = p \quad (2.11)$$

and the mixture variable,  $\bar{\phi}$ , can be defined as,

$$\bar{\phi} = \sum_{k=1}^2 \alpha^k \bar{\phi}^k. \quad (2.12)$$

Summing the equations 2.9 and 2.10 over all the phases, the governing filtered equations for the homogeneous mixture can be obtained as,

$$\frac{\partial}{\partial t}(\bar{\rho}) + \nabla \cdot (\bar{\rho} \tilde{\mathbf{u}}) = 0, \quad (2.13)$$

$$\frac{\partial}{\partial t}(\bar{\rho} \tilde{\mathbf{u}}) + \nabla \cdot (\bar{\rho} \tilde{\mathbf{u}} \otimes \tilde{\mathbf{u}}) + \nabla \cdot (\bar{\rho} \mathbf{I} - \bar{\boldsymbol{\tau}}) + \nabla \cdot (\tau_{sgs}) = 0. \quad (2.14)$$

One can note that the momentum equation for the mixture includes the sub-grid scale terms which should be modeled. Since by using homogeneous mixture approach, the above filtered equations are the same as the filtered governing equations for single-phase isothermal compressible flows, the subgrid scale modeling developed for these flows are often applied. In the following, two of these subgrid scale modeling which are used in this thesis, are presented.

### 2.1.2 ILES approach

In the ILES, implicit Large Eddy Simulation, approach, no explicit modeling is provided for the subgrid scale terms, and it is assumed that the numerical dissipation mimics the effect of these terms. This approach has been successfully applied in isothermal simulation of non-cavitating and cavitating flows [37, 42, 43, 44]. All of these studies have shown that the cavitation dynamics captured using the ILES compares well with the experimental high speed visualization. It should be also mentioned that ILES approach has been successfully applied to cavitating flows by Egerer et al. [24] although with different formulation compared to the one used in this thesis.

### 2.1.3 WALE approach

In the WALE approach [45], the sub-grid scale tensor,  $\tau_{sgs}$ , is written as,

$$\tau_{sgs} - \frac{2}{3} k_{sgs} \mathbf{I} = -2 \nu_{sgs} \bar{\mathbf{S}}, \quad (2.15)$$

where  $k_{sgs}$  is the sub-grid kinetic energy and  $\nu_{sgs}$  is the sub-grid scale turbulent viscosity which can be obtained from,

$$\nu_{sgs} = C_k \Delta \sqrt{k_{sgs}}. \quad (2.16)$$

In the above equation,  $\Delta$  is the cell length scale,  $C_k$ , the model constant, is assumed to be 1.6 and  $k_{sgs}$ , the sub-grid kinetic energy, can be calculated from,

$$k_{sgs} = \left( \frac{C_w^2 \Delta}{C_k} \right)^2 \frac{(\tilde{S}^d \tilde{S}^d)^3}{\left( (\tilde{S} \tilde{S})^{5/2} + (\tilde{S}^d \tilde{S}^d)^{5/4} \right)^2}, \quad (2.17)$$

where  $\tilde{S}$  and  $\tilde{S}^d$  are, respectively, the resolved-scale strain rate tensor and traceless symmetric part of the square of the velocity gradient tensor, and  $C_w$ , the model constant, is assumed to be 0.325.

## 2.2 CAVITATION MODELING

In order to solve the mixture governing equations (equations 2.13 and 2.14), they should be coupled with the proper cavitation modeling which takes into account the phase transition between liquid and vapor phases. In this thesis, two types of cavitation models are used and these models are explained in the following sections.

### 2.2.1 Transport equation based cavitation model

In these models, the cavitation dynamics is captured by solving a transport equation for the liquid volume fraction,  $\alpha^l$ . This equation can be obtained from equation 2.9 using the homogeneous mixture assumption (equation 2.11) as,

$$\frac{\partial}{\partial t}(\alpha^l \bar{\rho}^l) + \nabla \cdot (\alpha^l \bar{\rho}^l \bar{\mathbf{u}}) = \dot{m}, \quad (2.18)$$

where  $\dot{m}$  is the mass transfer term which accounts for vaporization and condensation. Here, the Schnerr-Sauer cavitation model [46] is used for this term. The mass transfer term is written as the summation of condensation,  $\dot{m}_{\alpha_c^l}$ , and vaporization,  $\dot{m}_{\alpha_v^l}$ , terms as,

$$\dot{m} = \alpha^l \left( \dot{m}_{\alpha_v^l} - \dot{m}_{\alpha_c^l} \right) + \dot{m}_{\alpha_c^l}, \quad (2.19)$$

where  $\dot{m}_{\alpha_v^l}$  and  $\dot{m}_{\alpha_c^l}$  are obtained from,

$$\dot{m}_{\alpha_c^l} = C_c \alpha^l \frac{3 \bar{\rho}^l \bar{\rho}^v}{\bar{\rho} R_B} \sqrt{\frac{2}{3 \bar{\rho}^l}} \sqrt{\frac{1}{|\bar{p} - p_v|}} \max(\bar{p} - p_v, 0), \quad (2.20)$$

$$\dot{m}_{\alpha_v^l} = C_v \left(1 + \alpha_{Nuc} - \alpha^l\right) \frac{3\bar{\rho}^l \bar{\rho}^v}{\bar{\rho} R_B} \sqrt{\frac{2}{3\bar{\rho}^l}} \sqrt{\frac{1}{|\bar{\rho} - p_v|}} \min(\bar{\rho} - p_v, 0). \quad (2.21)$$

In equations 2.20 and 2.21,  $C_c$  and  $C_v$  are set to 1,  $p_v$  is the vapor pressure,  $\alpha_{Nuc}$  is the initial volume fraction of nuclei, and  $R_B$  is the radius of the nuclei which is obtained from

$$R_B = \sqrt[3]{\frac{3}{4\pi n_0} \frac{1 + \alpha_{Nuc} - \alpha^l}{\alpha^l}}. \quad (2.22)$$

The initial volume fraction of nuclei is calculated from

$$\alpha_{Nuc} = \frac{\frac{\pi n_0 d_{Nuc}^3}{6}}{1 + \frac{\pi n_0 d_{Nuc}^3}{6}}, \quad (2.23)$$

where the average number of nuclei per cubic meter of liquid volume,  $n_0$ , and the initial nuclei diameter,  $d_{Nuc}$ , are assumed to be  $10^{12}$  and  $10^{-5}$  m, respectively.

### 2.2.2 Barotropic cavitation model

This type of cavitation models are mostly implemented in density-based solvers [1] where the governing equations are solved to obtain the conserved variables. These variables in equations 2.13 and 2.14 are  $\bar{\rho}$  and  $\bar{\rho}\tilde{\mathbf{u}}$ . In order to obtain the vapor fraction in the mixture of liquid and vapor, it is assumed that these two phases are in mechanical and thermodynamic equilibrium at every location in the flow. Using this equilibrium condition, the mixture density,  $\bar{\rho}$ , obtained by solving the governing equations, is considered as a weighted summation of vapor saturation density,  $\rho_{sat}^v$ , and liquid saturation density,  $\rho_{sat}^l$ ,

$$\bar{\rho} = \alpha^v \rho_{sat}^v + (1 - \alpha^v) \rho_{sat}^l, \quad (2.24)$$

where  $\alpha^v$  is the vapor volume fraction. By rearranging the above equation, the vapor volume fraction can be obtained from,

$$\alpha^v = \frac{\bar{\rho} - \rho_{sat}^l}{\rho_{sat}^v - \rho_{sat}^l}. \quad (2.25)$$

In order to close the system of equations, the pressure should be obtained using a proper barotropic equation of state where the pressure is assumed to depend only on density,

$$p = p(\rho). \quad (2.26)$$

For the pure liquid phase ( $\bar{\rho} > \rho_{sat}^l$ ), this barotropic equation of state is the Tait equation of state [47] with the assumption that the saturated density and pressure are constant. This equation reads,

**Table 2.1:** Parameters in equation 2.28, 2.25, and Tait equation of state (equation 2.27) for barotropic EOS.

$p_{sat}$	2340 <i>pa</i>	$B$	$3.06 \times 10^8$ <i>pa</i>
$\rho_{sat}^l$	998.2 <i>kg/m<sup>3</sup></i>	$\rho_{sat}^v$	0.01389 <i>kg/m<sup>3</sup></i>
$N$	7.1	$C$	1480 <i>Pakg/m<sup>3</sup></i>

$$\bar{p} = B \left[ \left( \frac{\bar{\rho}}{\rho_{sat}^l} \right)^N - 1 \right] + p_{sat}, \quad (2.27)$$

where  $N$  and  $B$  are constants. For the mixture phase ( $\bar{\rho} < \rho_{sat}^l$ ), the barotropic equation proposed by Egerer et al. [24] is used. This equation is derived by assuming that the vaporization/condensation process is isentropic and reads as,

$$\bar{p} = p_{sat} + C \left( \frac{1}{\rho_{sat}^l} - \frac{1}{\bar{\rho}} \right), \quad (2.28)$$

where  $C$  is a model constant. This constant together with other parameters in equations 2.25, 2.27, and 2.28 are defined in Table 2.1.

### 2.3 NUMERICAL EROSION ASSESSMENT

Two erosion assessment methods have been used in this thesis. These methods are explained in the following sections.

#### 2.3.1 Method based on compressible simulation

By considering the compressibility effect in the simulation, the collapse-induced shock waves can be captured. Since these shock-waves are one mechanism of cavitation erosion, their strength can be used to identify aggressive collapse events. In order to obtain the frequency and the location of these aggressive collapses, the collapse detector developed by Mihatsch et al. [2] is applied. This method detects collapse events and estimates their collapse strength based on the maximum pressure upon the collapse. The algorithm of this method can be summarized as follows:

- At each time step, a list of cells, called candidate cell list, is created with the conditions that the liquid fraction of the cell at the current time step should be one,  $\alpha^l = 1$ , and the liquid fraction at the previous time step should be less than 1,  $\alpha_{old}^l < 1$ . The cells in this list are considered as the candidate cells in which the collapse of a cavity has occurred.
- The cells in the candidate cell list that have neighboring cells filled with liquid are considered to contain the last stage of an isolated collapse event.



- The pressure at the cells containing the collapse events are recorded when the divergence of velocity changes its sign from negative to positive.
- Collapse strength is estimated based on the maximum pressure at the collapse centre,  $p_{collapse}$ .

Schmidt et al. [48] showed that the maximum pressure captured by the above algorithm is inversely proportional to the size of the cell at the centre of the collapse. In order to remove this dependency, Mihatsch et al. [2] introduced a scaled collapse pressure,  $p_{scaled}$ , based on the reference length scale,  $x_{ref}$ , and size of the cell at the centre of the collapse,  $\sqrt[3]{V_{cell}}$ , as

$$p_{scaled} = \frac{\sqrt[3]{V_{cell}}}{x_{ref}} p_{collapse}. \quad (2.29)$$

Note that  $x_{ref}$  in above equation is case and flow dependent and needs to be calibrated if the exact value of pressure at the centre of the collapse is of interest. However, our aim in this study is to identify the most aggressive collapse events in the same flow condition, therefore there is no need to know the exact value of  $x_{ref}$ . Here, we used  $p_{scaled} \cdot x_{ref}$  to scale the aggressiveness of collapse events.

### 2.3.2 Method based on incompressible simulation

In the incompressible simulation, the collapse-induced shock-waves cannot be captured, therefore the risk of cavitation erosion needs to be modeled based on other flow properties. In this thesis, a modeling is developed which is based on the energy description of cavitation erosion. This description, shown in Figure 2.1, considers that when a cavity is formed, its surrounding liquid gains potential energy. During the collapse of the cavity, most of this potential energy is transformed to kinetic energy carried by the inward motion in the liquid toward the centre of the collapse. At the end of the collapse, a fraction of the kinetic energy is transferred to the nearby surface by two mechanisms of cavitation erosion, micro-jets and shock-waves. The accumulation of energy in the surface eventually leads to cavitation erosion.

Based on this description of cavitation erosion, a new erosion assessment method is presented in Paper C. This method traces collapsing cavities during the simulation and estimates the kinetic energy in their surrounding liquid. The method then provides a modelling on how this kinetic energy is transferred to the surface either by considering a shock-wave or a micro-jet depending on where the collapse occurs. The accumulated surface energy can then be used as erosion indicator.

To estimate the kinetic energy around collapsing cavities, the surrounding liquid of these cavities is split into two volumes, the near-field and the far-field. The near-field volume,  $V_{I1}$ , contains the liquid inside the sphere or spherical cap shown in Figure 2.2b, while the far-field volume,  $V_{I2}$ , contains the liquid outside of this

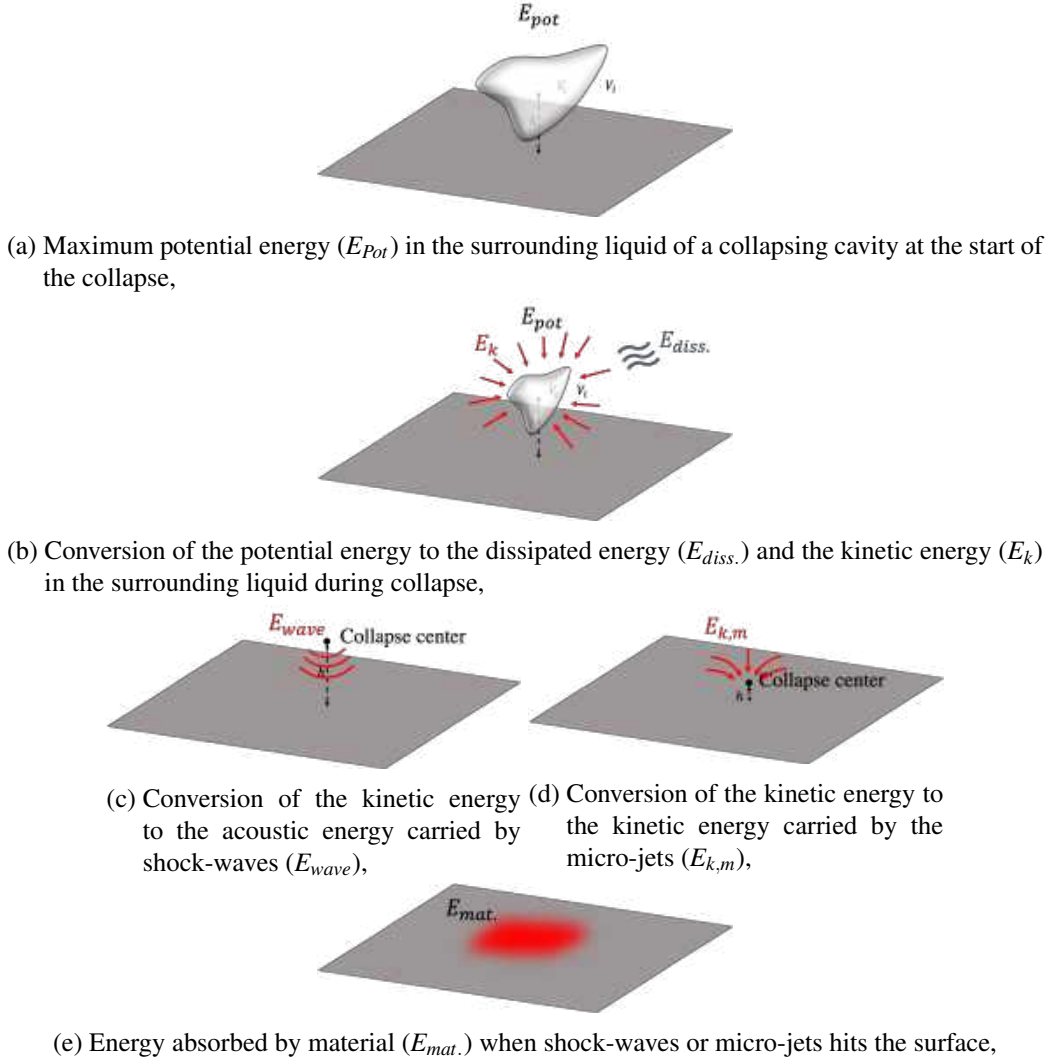


**Figure 2.1:** Energy-based description of cavitation erosion.

sphere or spherical cap. Based on the volume split, the kinetic energy in the surrounding liquid is split into the near-field kinetic energy,  $E_{k,1}$ , and the far-field kinetic energy,  $E_{k,2}$ ,

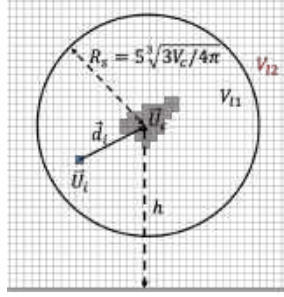
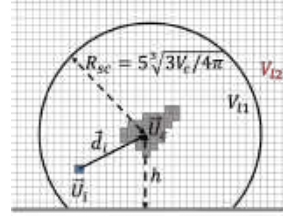
$$E_k = E_{k,1} + E_{k,2}. \quad (2.30)$$

The near-field kinetic energy is calculated directly from the flow properties in the cells located in the near field volume while the far-field kinetic energy is approximated with the assumption that the collapsed induced velocity in the far-field volume,  $U_r$ , is only a function of the distance from the centre of the cavity,  $r$ . The final form of the equation can be written as,

$$E_k \approx \sum_{i \in V_{l1}} \frac{1}{2} \rho_i V_i U_{r,i}^2 + \begin{cases} \rho_l \dot{V}_v^2 \left( \frac{1}{8\pi R_s} - \frac{1}{8\pi h} + \frac{\ln(2)}{4\pi h} \right) & h > R_s \\ \rho_l \dot{V}_v^2 \left( \frac{1}{4\pi h} \right) \ln\left(\frac{h+R_{sc}}{R_{sc}}\right) & h \leq R_{sc} \end{cases}, \quad (2.31)$$



(a) Collapsing cavity with an arbitrary shape,

(b) Volume split for  $h > 5\sqrt[3]{3V_c/4\pi}$ (c) Volume split for  $h \leq 5\sqrt[3]{3V_c/4\pi}$ **Figure 2.2:** Volume split of the surrounding liquid of a collapsing cavity.

where the first term in the right hand side is the near field kinetic energy and the second term is the far-field kinetic energy. In equation 2.31,  $\rho_i$ ,  $V_i$ , and  $U_{r,i}$  are, respectively, the density, the volume, and the collapse induced velocity in the cell  $i$  located in the surrounding liquid,  $\rho_l$  is the liquid density,  $\dot{V}_v$  is the time derivative of vapor content in the cloud cavity,  $h$  is the normal distance between the centre of the cavity and the nearest wall, and  $R_s$  and  $R_{sc}$  are, respectively, the radius of the sphere and spherical cap used for volume splitting in Figure 2.2. Here, it is assumed that  $R_s$  and  $R_{sc}$  are five times larger than the radius of sphere with the same volume as the collapsing cavity. For the detailed derivation of equation 2.31, the reader is referred to Paper C which is attached to this thesis.

Based on the energy description of cavitation erosion, the kinetic energy induced by the collapse in the surrounding liquid is transferred to the nearby surface at the end of collapse. According to Ochiai et al. [28], two mechanisms of cavitation erosion, shock-waves or micro-jets, can be responsible for this energy transfer depending on the initial stand-off ratio,  $\gamma$ , of collapsing cavities. This ratio is defined as,

$$\gamma = h / \sqrt[3]{3V_0/4\pi} \quad (2.32)$$

where  $h$  is the distance between the cavity and the wall and  $V_0$  is the initial volume of the cavity.

For the cavities with  $\gamma \geq 3.0$ , it is assumed that the collapse induced kinetic energy in the surrounding liquid is transformed to the acoustic energy in shock-waves. Upon the impact of these shock-waves on the surface, a fraction of their acoustic energy is transmitted to the surface. Following the work by Schenke and van Terwisga [49], this fraction can be calculated using a continuous form of the

solid angle projection as,

$$E_{mat.,j} = \frac{1}{4\pi} \left( \frac{\vec{d}_{i,j} \cdot \vec{n}_j}{|\vec{d}_{i,j}|^3} \right) A_j E_{k,max,i} \quad (2.33)$$

where  $E_{mat.,j}$  is the transferred energy to the surface element  $j$ ,  $\vec{d}_{i,j}$  is the vector connecting the centre of the surface element and the centre of the collapse,  $\vec{n}_j$  is the normal unit vector of the surface element,  $A_j$  is the area of the surface element and  $E_{k,max,i}$  is the maximum kinetic energy induced by the collapse in the surrounding liquid.

For the collapsing cavities with  $\gamma = 0$ , the kinetic energy in the surrounding liquid is assumed to be converted to kinetic energy in the induced micro-jets. When these micro-jets hit the surface, they transfer their kinetic energy to the surface. It is assumed that the surface hit by micro-jets includes the surface elements covered by the approximate projected area of the cavity on the nearby surface,  $A_{proj,i}$ . Considering this assumption, the amount of energy transferred to the surface element  $j$  through micro-jets can be approximated from,

$$E_{mat.,j} = \begin{cases} \frac{E_{k,max,i} A_j}{A_{proj,i}} & |d_{i,j}| < \sqrt{(\frac{3V_{0,i}}{4\pi})^{2/3} + h_{i,j}^2} \\ 0 & |d_{i,j}| \geq \sqrt{(\frac{3V_{0,i}}{4\pi})^{2/3} + h_{i,j}^2} \end{cases}, \quad (2.34)$$

where  $h_{i,j}$  is the normal distance between the collapse centre of cavity  $i$  and the surface element  $j$ .

For the cavities with  $0 < \gamma < 3.0$ , both shock-waves and micro-jets are considered to be responsible for the energy transfer between the collapse centre and the nearby surface; therefore the absorbed energy by the surface element,  $j$ , is obtained from,

$$E_{mat.,j} = \frac{1}{4\pi} \left( \frac{\vec{d}_{i,j} \cdot \vec{n}_j}{|\vec{d}_{i,j}|^3} \right) A_j E_{ac,i} + \begin{cases} \frac{E_{km,i} A_j}{A_{proj,i}} & |d_{i,j}| < \sqrt{(\frac{3V_{0,i}}{4\pi})^{2/3} + h_{i,j}^2} \\ 0 & |d_{i,j}| \geq \sqrt{(\frac{3V_{0,i}}{4\pi})^{2/3} + h_{i,j}^2} \end{cases}, \quad (2.35)$$

where  $E_{ac,i}$  and  $E_{km,i}$  are, respectively, the acoustic energy in shock-waves and the kinetic energy in the micro-jets due to collapse of cavity  $i$ . To determine the amount of these energies, it is assumed that the surrounding liquid is linearly divided between the kinetic energy in the micro-jet and the acoustic energy of the shock-wave based on the stand-off distance of the cavity,

$$E_{km,i} = (1 - \frac{\gamma}{3.0}) E_{k,max,i}, \quad E_{ac,i} = \frac{\gamma}{3.0} E_{k,max,i}. \quad (2.36)$$

The indicator of cavitation erosion risk is defined based on study by Okada et al. [50] and the numerical study by Fortes-Patella et al. [51] who showed that

there is a linear relationship between the volume loss due to cavitation erosion after the incubation period and the total energy stored in the eroded surface. Using this linear relationship, an indicator of cavitation erosion risk for the surface element,  $j$ , can be defined as,

$$EI_j = \frac{1}{t_s} \sum_{i=1}^{n_i} \frac{E_{mat.,j,i}}{A_j}, \quad (2.37)$$

where  $t_s$  is the simulation time and  $n_i$  is the number of collapse events detected during the simulation. It should be noted that in equation 2.37, the total absorbed energy is divided by the simulation time and the area of the surface element to make the defined erosion indicator independent of these two parameters.



---

# 3

## *Studied cases*

---

In this chapter, the cases studied in this thesis are briefly described. The results for these cases are presented in the summary of the papers in the next chapter. The description of each case include the experimental set-up, the numerical computational domain, the topology of mesh and its resolution, and studied flow conditions.

### **3.1 NACA0009 FOIL**

In order to investigate the shedding mechanisms of cavitating structures from leading-edge cavitation which are associated with high risk of cavitation erosion, the leading edge cavitation formed on the modified NACA0009 foil is studied using both experimental and numerical methods. In the following subsections, the experimental set-up and the computational domain in the simulations are briefly presented.

#### *3.1.1 Experimental set-up*

The experiments were performed in the EPFL high-speed cavitation tunnel (see Figure 3.1a). The test section has dimensions  $0.15 \times 0.15 \times 0.75 \text{ m}^3$ . The foil was placed in the cavitation tunnel at the incidence angle  $\alpha = 5^\circ$  and the inlet velocity and the cavitation number are, respectively, set to  $U = 20 \text{ m/s}$  and  $\sigma = 1.25$ . The foil has a chord length,  $C$ , of 100 mm and a span length of 150 mm. The geometry of the foil can be described by the following equations, where  $x$  and  $y$  stand for the stream-wise and vertical coordinates respectively,

$$\frac{y}{C} = \begin{cases} a_0 \left(\frac{x}{C}\right)^{\frac{1}{2}} + a_1 \left(\frac{x}{C}\right) + a_2 \left(\frac{x}{C}\right)^2 + a_3 \left(\frac{x}{C}\right)^3 & 0 \leq \frac{x}{C} \leq 0.45 \\ b_1 \left(1 - \frac{x}{C}\right) + b_2 \left(1 - \frac{x}{C}\right)^2 + b_3 \left(1 - \frac{x}{C}\right)^3 & 0.45 \leq \frac{x}{C} \leq 1 \end{cases} \quad (3.1)$$

**Table 3.1:** Coefficients,  $a$  and  $b$ , in equation 3.1.

$a_0$	+0.173688	$b_1$	+0.1737
$a_1$	0.244183	$b_2$	0.185355
$a_2$	+0.313481	$b_3$	+0.33268
$a_3$	0.275571		

In the above equation, the coefficients  $a_i$  and  $b_i$  are given in Table 3.1.

The dynamics of cavitation was recorded by a high-speed camera (Photron FASTCAM mini) from the top view. In order to have videos with high frame rates and very sharp images, two measures regarding the camera setting were taken. First, the camera view was focused to the middle half of the foil which enabled us to increase the frame rate of the recorded video to 10 kHz. Secondly, by using an excessive amount of light, we were able to reduce the exposure time for each frame to 1/150000 s which resulted in very sharp and clean images in the recorded videos.

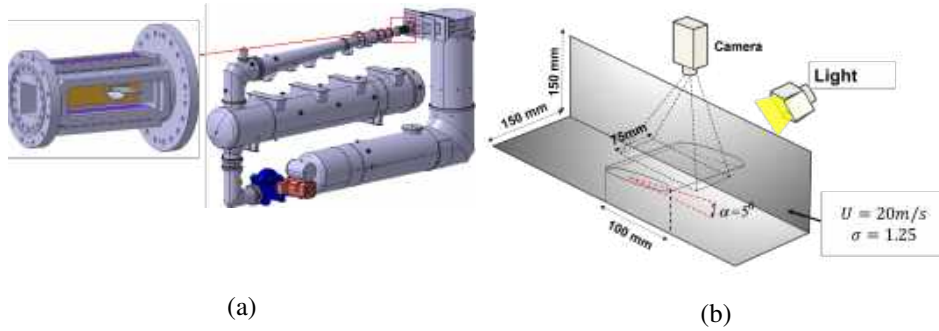


**Figure 3.1:** A schematic view of a) EPFL high-speed cavitation tunnel, and b) the experimental set-up and operating conditions.

In order to locate aggressive collapses in the experiment, the so called paint test method is used where a thin layer of soft stencil ink is applied to the foil surface. The status of this layer after the cavitation test indicates the location of the aggressive collapse events as these events remove the ink from the foil. In order to apply the ink on the surface of the foil, we dipped the foil vertically along its span-wise axis into a container filled with Marsh Rolmark Roller Stencil Ink. The foil was then allowed to dry in the same position at room temperature for a couple of hours. The status of the paint after it dried is shown in Figure 3.2a. In order to check if the applied ink layer is uniform, we measured the layer thickness using Elcometer 456 Coating Thickness Gauge. Figure 3.2b shows the distribution of the ink layer thickness measured within the white box in Figure 3.2a. This distribution shows that the standard deviation of the paint layer thickness up to the 70



percent of the span is  $1 \mu\text{m}$  which is less than the accuracy of the device. This standard deviation is  $3 \mu\text{m}$  in the region from 70 percent of the span to the tip of the foil which is larger than the calculated and reported accuracy of the device. It can be concluded from this thickness measurement that the thickness of the ink layer is roughly uniform from root up to 70 percent of the span and that the average thickness of the ink layer in the rest of the foil increases rapidly toward the tip of the foil. This thickness distribution should be taken into account when one looks at the paint test results. In order to make sure that the paint removal seen after the cavitation test is only due to the collapse events and not the shear of the liquid flow, the coated foil is tested at the flow velocity of 20 m/s and non-cavitating condition for 30 minutes. As no paint removal due to the flow shear was observed, it can be concluded that only the collapse events are responsible for the paint removal in the cavitating conditions.

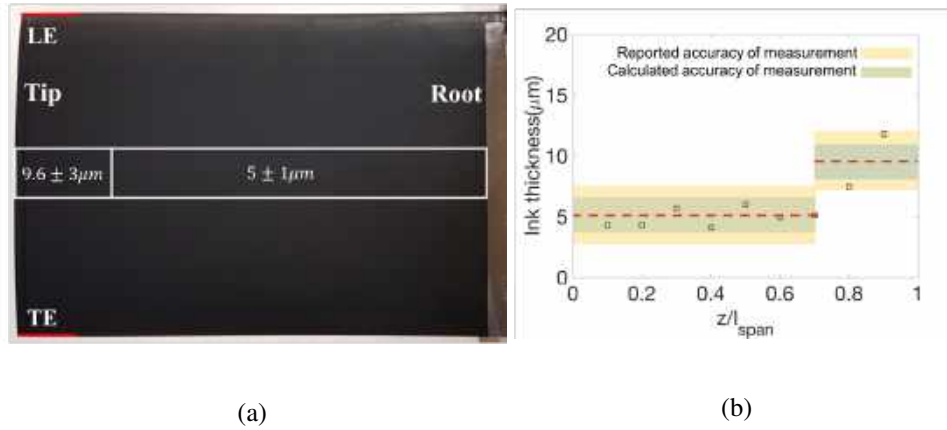


**Figure 3.2:** a) Status of the ink layer before cavitation test and b) the thickness of the ink layer measured within the box (a). (In (b),  $z/l_{span}$  is zero at the root and one at the tip).

### 3.1.2 Computational domain

Figure 3.3a shows the computational domain and boundary conditions for the simulations. The domain consists of a 3D channel with the same height as the test section shown in Figure 3.1b. The width of domain is equal to one-third of the foil span to decrease the computational cost. In the stream-wise direction, the domain is extended 4C upstream of the foil leading edge and 6C behind of the trailing edge. For the side walls in the simulation, slip boundary conditions for velocity and zero gradient conditions for pressure and vapor fraction are used. For the top and bottom walls, we used no-slip boundary condition for velocity and zero gradient for other flow variables. The topology of the mesh around the foil is shown in Figure 3.3b. The mesh is divided into two regions with different types of mesh. The region near the foil is discretized with a structured hexahedral O-type

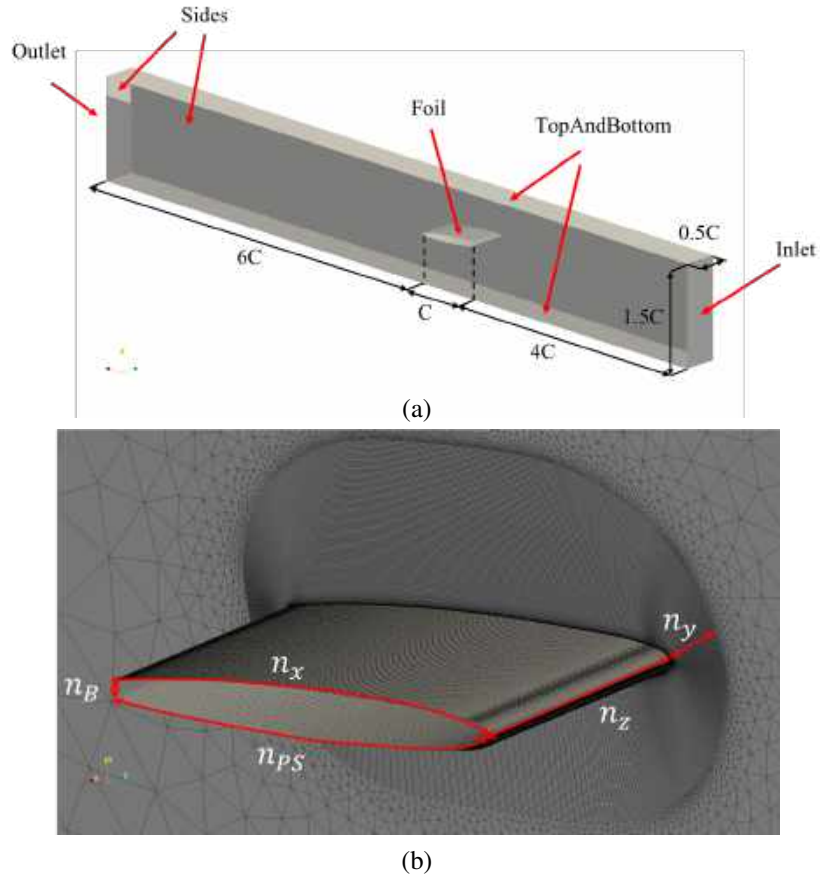


**Figure 3.3:** Computation configuration for the foil, a) computation domain and b) grid topology.

**Table 3.2:** Specifications of the grid used for the simulation ( $n_x$ ,  $n_y$ ,  $n_z$ ,  $n_{PS}$ , and  $n_B$  are defined in figure 3.3b and  $n_{total}$  is the total number of the cells).

Grid	$n_x$	$n_y$	$n_z$	$n_{PS}$	$n_B$	$n_{total}$
$G1_{vis.}$	170	86	70	140	10	2.16M
$G2_{vis.}$	340	131	140	140	10	9.76M
$G1_{invis.}$	340	96	140	140	10	7.35M

mesh, and the outer region is discretized with an unstructured mesh. Three grids with different mesh resolutions are created. Table 3.2 shows the specifications of these grids. In this table, the first two grids,  $G1_{vis.}$  and  $G2_{vis.}$ , are used in the incompressible viscous simulations while the third grid,  $G1_{invis.}$  is used in the compressible inviscid simulation.

### 3.2 AXISYMMETRIC CAVITATING NOZZLE FLOW

In order to validate the numerical erosion assessment methods developed in this thesis, the cavitating flow in an axisymmetric nozzle is simulated. This configuration is the same as the experimental set-up by Franc et al. [3] in which the cavitation erosion is investigated. A schematic view of the flow configuration is shown in Figure 3.4a. The configuration consists of a converging nozzle connected to a pipe and a disk. The flow passes through the nozzle and the pipe and it is then deflected by the lower wall of the disk placed 2.5 mm away from the pipe exit. Due to this deflection, the flow experiences a sharp turn which leads to a pressure drop. This pressure drop then results in the formation of a sheet cavity attached to the upper wall of the disk. The computational domain and the mesh topology are shown in Figure 3.4b. In order to reduce the computational cost, the domain includes only 1/8 of the geometry with a symmetry boundary condition used for the side planes. The same approach is used in the numerical study by Gavaises et al. [52]. The flow rate at the inlet and the pressure at the outlet is set according to the experiments by Franc et al. [3]. With this flow rate and pressure, the cavitation number,  $\sigma$ , is set to 0.9. To study the effect of mesh resolution on the risk of cavitation erosion predicted by the developed method, three grids with different mesh resolutions are used in the simulations. The specification of these grids in the region where the sheet cavitation is formed, are shown in Table 3.3. In all three mesh resolutions, the averaged non-dimensional wall distance,  $y^+$ , is around 1 while the averaged non-dimensional stream-wise distance in the cavity region,  $x^+$ , varies from 700 to 350.

**Table 3.3:** The description of the mesh used for the cavitating flows in the axisymmetric nozzle.

Grids	$n_1$	$n_2$	$n_3$	$n_{total}$
CM	25	41	43	242k
MM	37	61	65	661K
FM	47	80	85	1623k

### 3.3 WATER-JET PUMPS

In this thesis, two water-jet pumps were investigated using an LES approach with two objectives. The first objective is to identify the mesh resolution required to capture the main features of the flow in water-jet pumps. For this objective, the AxWJ-2 water-jet pump [40] is selected as extensive experimental data are available for this pump in the literature. The second objective is to investigate numerically the risk of cavitation erosion in a commercial pump. This investigation is performed on a mixed-flow water-jet pump from Kongsberg maritime. In the fol-

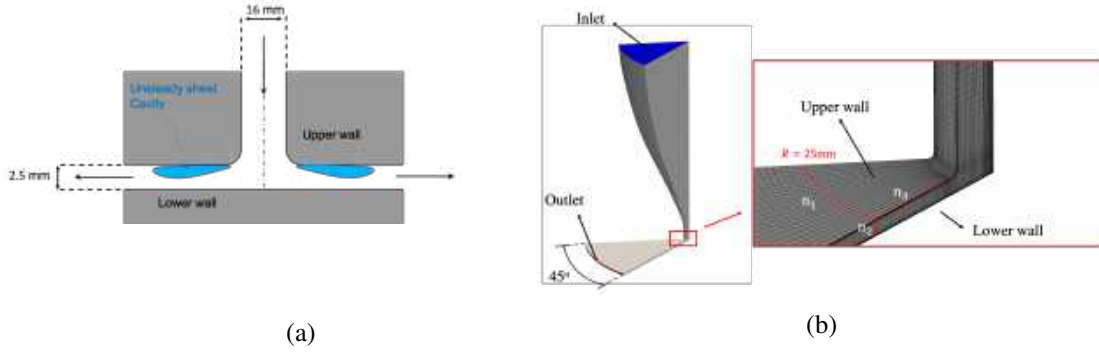


**Figure 3.4:** Configuration for an axisymmetric nozzle stagnation flow, a) schematic view of the configuration and the expected cavitation pattern seen in the experiment, b) computational domain and mesh topology.

lowing sections, these pumps and the mesh resolutions used for these simulations are presented.

### 3.3.1 AxWJ-2 water-jet pump

The AxWJ-2 water-jet pump is an axial pump with six rotor blades and eight stator blades. Figure 3.7b and Table 3.4 present, respectively, a schematic view of the pump and a summary of relevant data for this pump. As it can be seen in Table 3.4, the actual tip clearance where the measurements are done, is 0.9 mm while the nominal tip clearance is 0.7 mm. This difference is due to the eccentricity between the rotor and the shroud in the experiment according to Li et al. [41]. Simulating the configuration with the same eccentricity as the experiment is not computationally affordable as it requires running the simulation for a large number of revolutions to achieve statistical convergence. As a remedy, the diameter of the shroud in the simulation is expanded by 0.4 mm so that the tip clearance is 0.9 mm for all the blades during one revolution. This difference between the experimental and numerical geometries should be considered while comparing the numerical results with the experiment.

Figure 3.7a shows the computational domain used in this study. The computational domain is extended  $10D_1$  upstream and downstream of the pump to reduce the interaction between the flow in the pump and the inlet and outlet boundary conditions. The domain is divided into three regions, inlet\_pipe, rotor, and stator\_outlet\_pipe. Cyclic AMI interfaces are used for the boundaries between these regions. For the inlet\_pipe, a fully structured grid is used and the mesh is refined near the casing and the shaft to capture the boundary layers near these surfaces. The tangential resolution is, however, not fine enough for a wall-resolved LES. The mesh in the rotor and stator is divided into two regions with different types of mesh. The regions near the rotor blades, the hub, and the shroud are discretized with a structured hexahedral mesh, and the region in the middle of the passage

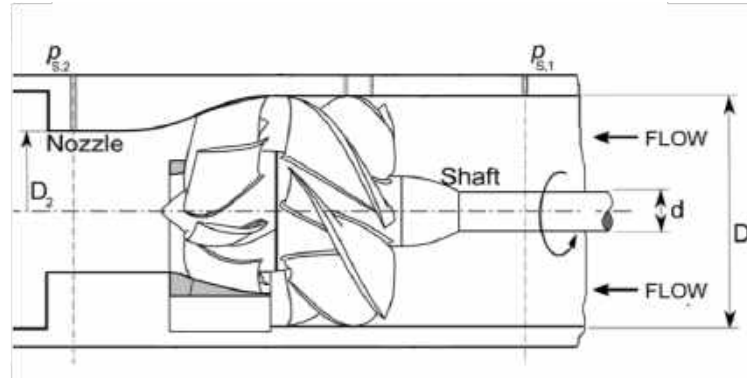


**Figure 3.5:** Sketch of the AxWJ-2 axial water-jet pump [14].

is discretized with an unstructured mesh. The mesh topology in the rotor region is shown in Figure 3.6b. In order to study the effect of mesh resolution, three base-line grids for the rotor region, CM, MM, and FM (described in table 3.5), are created. These grids have, respectively, 1.9, 5.0, and 12.5 million cells. To further increase the mesh resolution in the tip leakage region, the resolution of this region in the FM mesh is refined locally using the refineHexMesh utility in OpenFOAM. The refinement is performed around one blade (FMRefOne in table 3.5) and all of the blades (FMRefAll in Table 3.5). The refinement zone covers the tip of blade from  $r/R = 0.8$  to  $r/R = 1.0$  and in case of refinement around one blade, it is extended angularly 50 degrees in the suction side and 30 degrees in the pressure side direction of the selected blade (see Figure 3.6b). Table 3.5 presents the grid specifications for each grid. Note that  $n_r$  and  $n_c$  are the number of the grids on the blade in radial and chord-wise directions and  $y^+$  is non-dimensional wall distance of the first cell on the blade based on the tip velocity of the blade and the diameter of the rotor.

**Table 3.4:** Summary of relevant data for AxWJ-2 axial water-jet pump.

$D_1$	305.2 mm
$D_2$	213.4 mm
$D_{rotor}$	303.8 mm
Number of rotor blades $n_R$	6
Number of stator blades $n_S$	8
Nominal tip clearance h	0.7 mm
Actual tip clearance h	0.9 mm

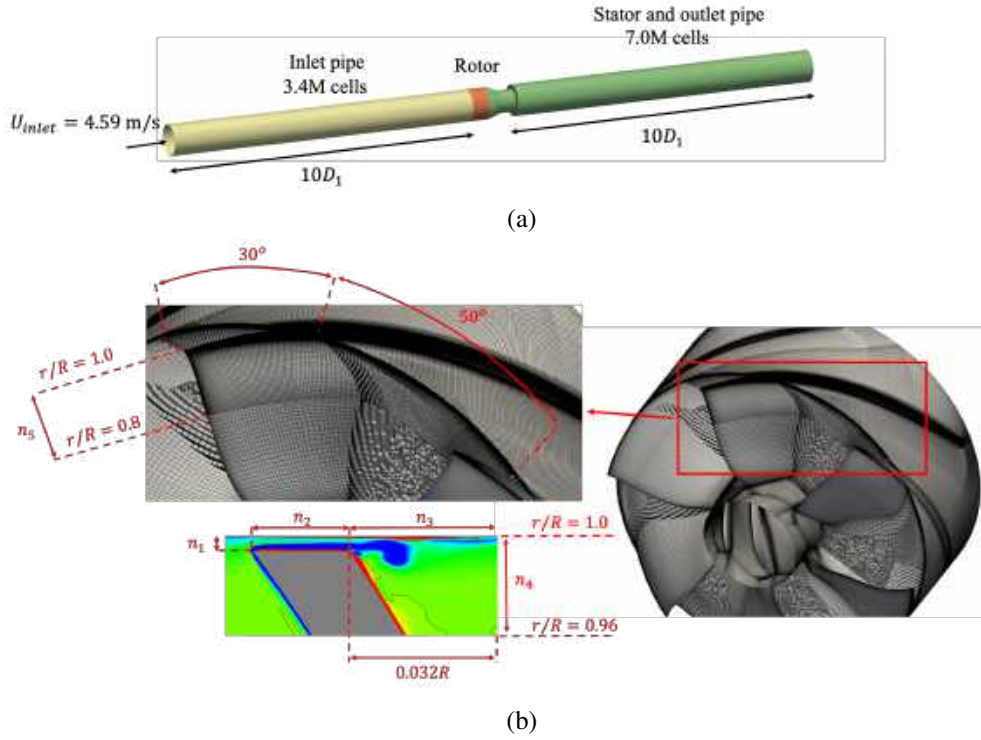


**Figure 3.6:** (a) Computational domain and (b) Mesh topology in the rotor region.

**Table 3.5:** Description of the grids in rotor region.

Grids	Size	$n_1$	$n_2$	$n_3$	$n_4$	$n_5$	$n_r$	$n_c$	$y^+$
CM	1.9M	10	10	8	14	39	56	58	180
MM	5.0M	15	15	12	21	53	75	84	135
FM	12.5M	20	20	16	28	68	104	116	90
FMRefAll	46.6M	40	40	32	56	136	152	232	45
FMRefOne	19.7M	40	40	32	56	136	152	232	45

### 3.3.2 Kongsberg water-jet pump

This water-jet pump has been experimentally studied in the water-jet system test set-up at Kongsberg Hydrodynamic Research Centre (KHRC). This set-up which is the same as the computational domain used in the simulation, is shown in Figure 3.7a. It consists of an inlet channel, a flush-type intake duct, a pump, and an outlet channel. The flow enters the set-up at the start of the inlet channel and exits from the outlets of the inlet and outlet channels. At the entrance of the intake duct, a fraction of the flow fed into the inlet channel enters the duct and passes through the pump where its head increases. This fraction of the flow is

then discharged to the outlet channel. Figure 3.7b shows the sketch of the pump which is a mixed-flow pump designed by Kongsberg Maritime. This pump has six rotor blades and eleven stator blades and the diameters of the pump inlet, rotor blades and the outlet nozzle are, respectively,  $D_1 = 200$  mm,  $D_r = 263.4$  mm, and  $D_2 = 130$  mm. Two flow conditions are studied which are associated with different risk of cavitation erosion according to the paint tests performed at KHRC. The description of these flow conditions are presented in Table 3.6. In this table,  $U_{inlet}$ ,  $\sigma$ , and  $n_M$  are, respectively, the averaged velocity at the inlet in Figure 3.7a, the cavitation number defined based on pressure at the outlet of the pump, and the shaft speed.

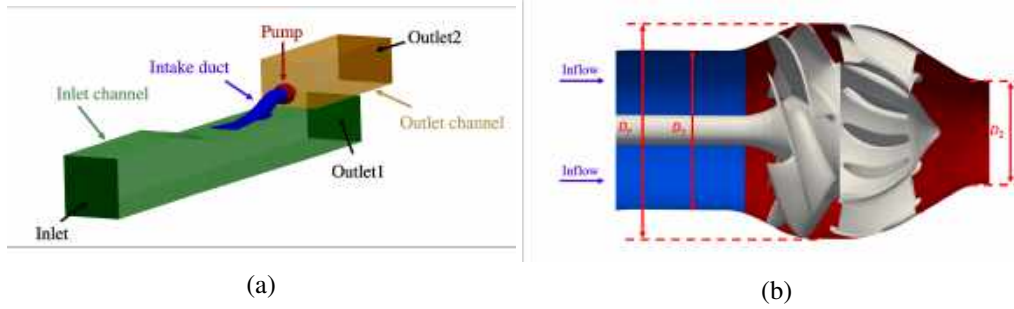


**Figure 3.7:** (a) Computational domain and (b) Sketch of the studied mixed-flow water-jet pump.

**Table 3.6:** Description of the studied flow conditions.

Conditions	$U_{inlet}$ (m/s)	$\sigma$	$n_M$ (rps)
C1	4.58	1.55	20
C2	6.64	0.67	20

The computational mesh in all components shown in Figure 3.7a is of a hybrid structured-unstructured type. The regions near the wall are meshed with structured grids while unstructured grids are used for the regions far from the walls. The topology and specification of the mesh in the rotor region of the pump are presented in Figure 3.8 and Table 3.5. The base-line mesh, BL in Table 3.7, is created using Pointwise V18.3 grid generation software and it consists of around 10 million cells. To further increase the mesh resolution while keeping the computational cost to a reasonable level, the mesh near one blade is refined using the refineHexMesh utility in OpenFOAM. The resultant mesh is named RefOne in Table 3.7. The total number of the cells in the domain is 33.5 million. It should be mentioned that the procedure of creating the mesh and the mesh resolution around the refined blade is the same as ones used in the simulation of the AxWJ-2 water-jet pump. In paper D, it is shown that this meshing procedure and mesh resolution are enough for capturing the main features of non-cavitating and cavitating flows in water-jet pumps.

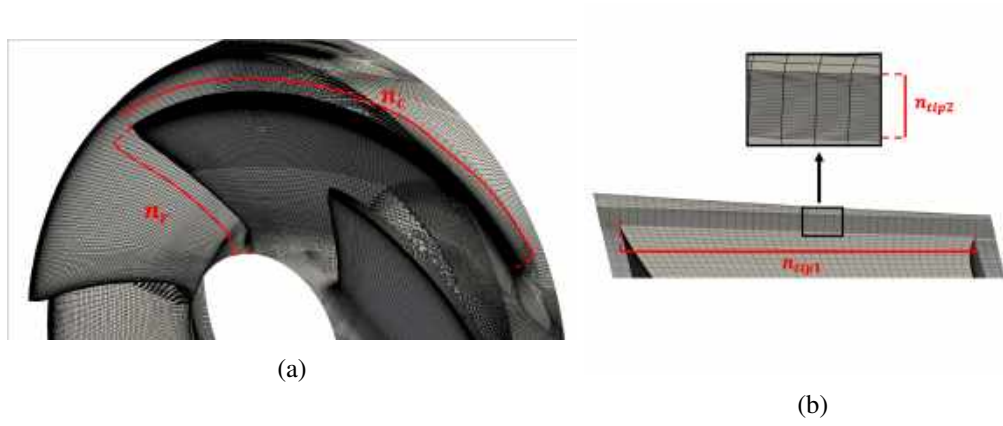


**Figure 3.8:** Mesh topology in the rotor region of the pump, a) surface mesh on the suction side of the rotor blade, b) mesh in the tip gap region.

**Table 3.7:** Description of the grids in rotor region.

Mesh	$n_c$	$n_r$	$n_{tip1}$	$n_{tip2}$	$n_{total}$
BL	116	119	20	20	10.3M
RefOne	232	211	40	40	16.1M



---

# 4

## *Summary of appended papers*

---

In this chapter, summaries of appended papers are presented. Each summary includes the objective of the paper and its main results.

### **4.1 PAPER A**

In this paper, the leading edge cavitation formed on the NACA0009 foil is investigated using numerical and experimental methods with the objective to identify the mechanisms generating transient cavities. As these transient cavities may undergo violent collapses leading to erosion, knowing their generation mechanisms can provide a better understanding of the erosion process. Both numerical and experimental investigations in this paper have indicated that there exists two shedding mechanisms of transient cavities: (a) Primary shedding, characterized by a periodic generation of large cloud cavities, (b) Secondary shedding of small-scale horse-shoe vortices from the sheet and the cloud cavity.

The primary shedding, shown in Figure 4.1, is the shedding of large-scale cloud cavities from the leading edge due to re-entrant jet. At each cycle of this shedding, a re-entrant jet (re-entrant jet 1 in Figure 4.1a) initiates from the closure line of the sheet cavity due to the high pressure gradient in the closure region. This re-entrant jet travels upstream and pinches off a large scale cloud cavity from the leading edge. The results in Figure 4.1b also show that while the sheet cavity is growing after the pinch off, another re-entrant jet initiates at the closure line of the growing cavity. This re-entrant jet is named secondary re-entrant jet in Figure 4.1b. In order to show the generation mechanism of the secondary re-entrant jet, the velocity vectors and the pressure field on the plane where this re-entrant jet is formed are shown in Figure 4.1c. In the instance  $t_1 + 6T/14$  which is prior to the formation of secondary re-entrant jet, a local pressure increase can be seen in the region between the closure line of the growing sheet cavity and the rolling cloud cavity. In Paper A, it is shown that this pressure increase is due the collision

between the flow rotating around the cloud cavity and the flow coming from the upstream. Due to this increased pressure, the pressure gradient at the closure line increases which eventually leads to the formation of a secondary re-entrant jet. This re-entrant jet can be observed in the velocity vectors at time  $t_1 + 2T/4$ .

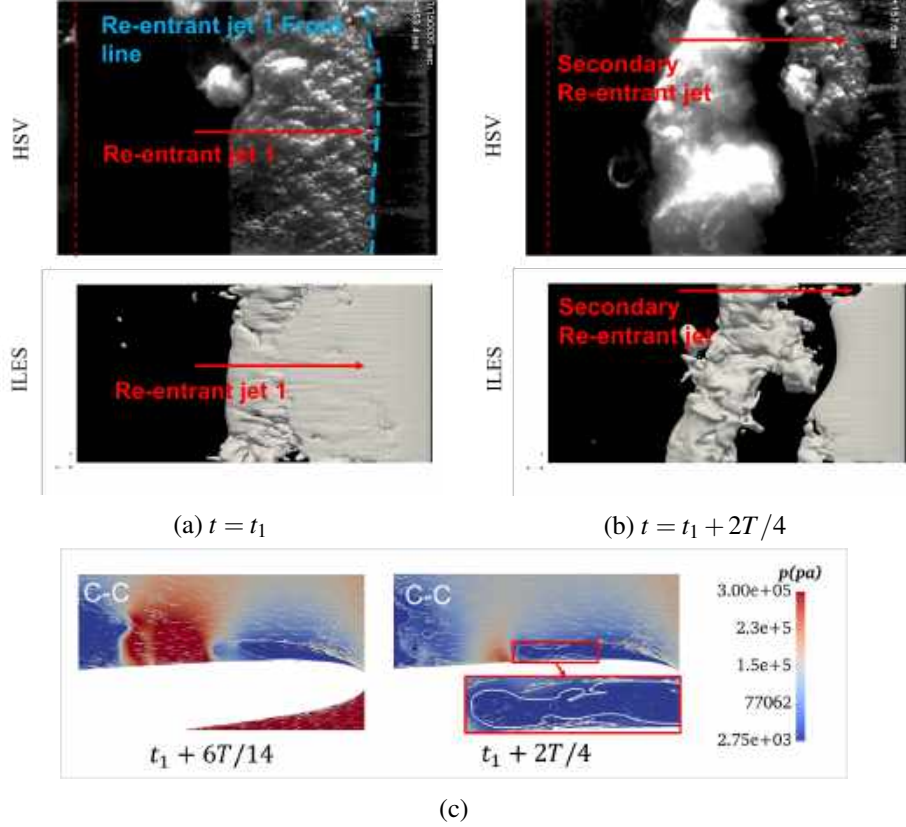


**Figure 4.1:** Primary shedding and the formation of re-entrant jets in HSV and numerical simulation (Flow is from right to left and  $T$  is the period of shedding).

The secondary shedding is the detachment of small-scale cavity structures from the sheet cavity and downstream end of the cloud cavity. Based on detail analysis of numerical simulation and High Speed Videos (HSV), three types of transient cavity structures can be created in this type of shedding. The first type is the cavity structure detached from the closure line of the sheet cavity when it has its maximum length. The detachment of this structure, CS1, is shown in Figure 4.2. In these instances, the main re-entrant jet has started from the closure line of the sheet cavity and is traveling upstream. The front-line of the re-entrant jet is shown by the blue dashed line in Figure 4.2. At the closure region, the interface of the sheet cavity is disturbed due to its interaction with the re-entrant jet. This interaction can be seen from velocity vectors and the interface of the sheet cavity on plane C-C in Figure 4.2. Due to this interaction, a small structure is detached from the closure line which eventually transforms into a horse-shoe cavitating structure as it travels downstream.

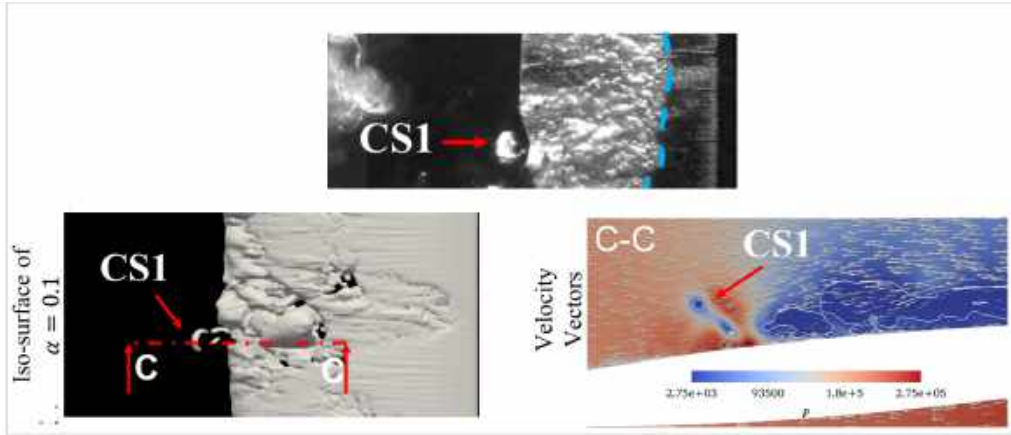


**Figure 4.2:** Detachment of structure CS1 due to an interaction between re-entrant jet and closure line of sheet cavity (Flow is from right to left).

The second type of structures from the secondary shedding is cavities detached from the closure line of the growing sheet cavity. This detachment in the numerical simulations and HSV is shown in Figure 4.3. At instance  $t_3 + T/7$  in the simulation results, a secondary re-entrant jet is created at the closure line of the growing sheet cavity. The mechanism for the creation of this re-entrant jet is discussed earlier. When this re-entrant jet reaches the leading-edge, it creates disturbance on the interface of the growing sheet cavity. This disturbance becomes larger as the sheet cavity grows and finally detaches at the instance  $t_3 + 3T/7$  from the closure line as the structure CS2.

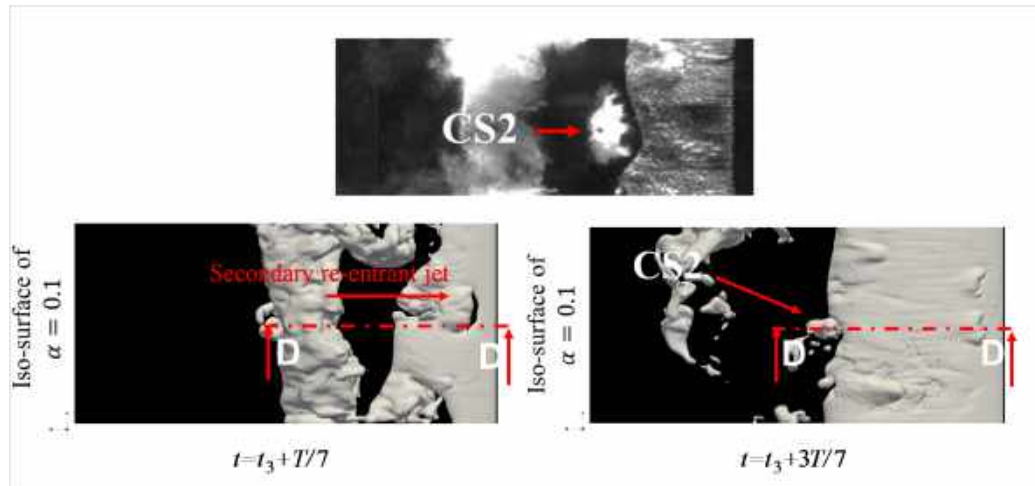


**Figure 4.3:** Detachment of structure CS2 from the closure line of the growing sheet cavity (Flow is from right to left).

The third type of structures in the secondary shedding is cavitating structures formed at the downstream end of the cloud cavity. Figure 4.4 shows the formation of this structure, CS3, in the numerical simulations and HSV. The iso-surface of  $Q$  criteria indicates that several three-dimensional vortical structures exist in the upper surface of the cloud. These structure have different velocity according to the velocity vector on the planes E-E in Figure 4.4. Due to this velocity difference, the upstream structures with high velocity merge with the low speed downstream vortical structures and form CS3 structures.

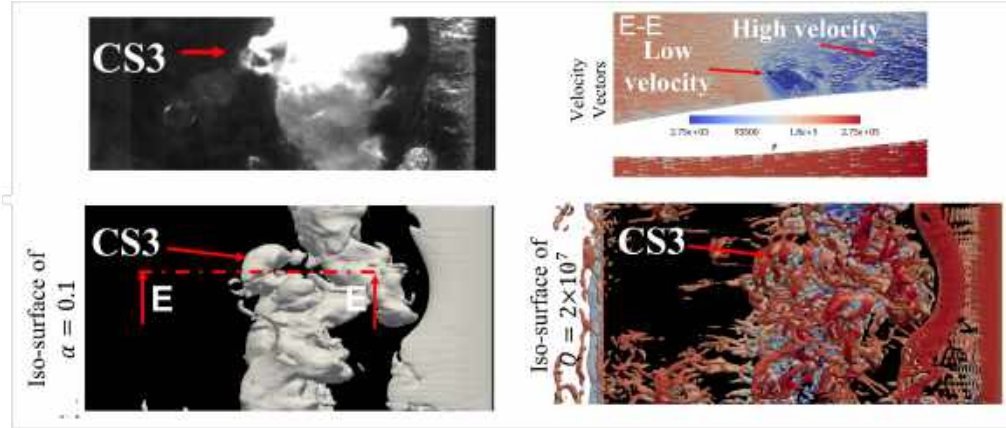


**Figure 4.4:** Detachment of structure CS3 from the downstream end of the cloud cavity (Flow is from right to left).

## 4.2 PAPER B

As the shedding mechanisms explained in Paper A create transient cavities which can collapse near the surface and cause erosion, the aggressiveness of these transient cavities is investigated in Paper B using experimental and numerical methods. Both compressible simulation and experimental paint test are used to identify the location of aggressive collapses. The numerical results and HSV are investigated to find the relation between the aggressive collapse events and shedding mechanisms.

Figure 4.5a presents the location of aggressive collapse events identified using paint test. These events occur in four distinctive regions: (1) a very narrow strip of paint removal on the leading edge of the foil; (2) a region around 60 percent of the sheet cavity maximum length; (3) a region around the closure line of the sheet cavity at its maximum length; and (4) a dispersed region close to the trailing edge of the foil. The compressible simulation results in Figure 4.5b and 4.5c show that the above mentioned four regions are also present in the distribution of maximum surface pressure on the foil and the collapse locations. It can also be seen in these figures that there are several collapse events in region 4, which do not induce high

pressure pulses on the surface of the foil. The side view of Figure 4.5c shows that these collapse events are far away from the surface, therefore their resultant shock waves decay before reaching the surface of the foil and are not able to produce high pressure pulses on the surface. This observation can explain the reason for the lower risk of cavitation erosion in region 4 compared to region 3.

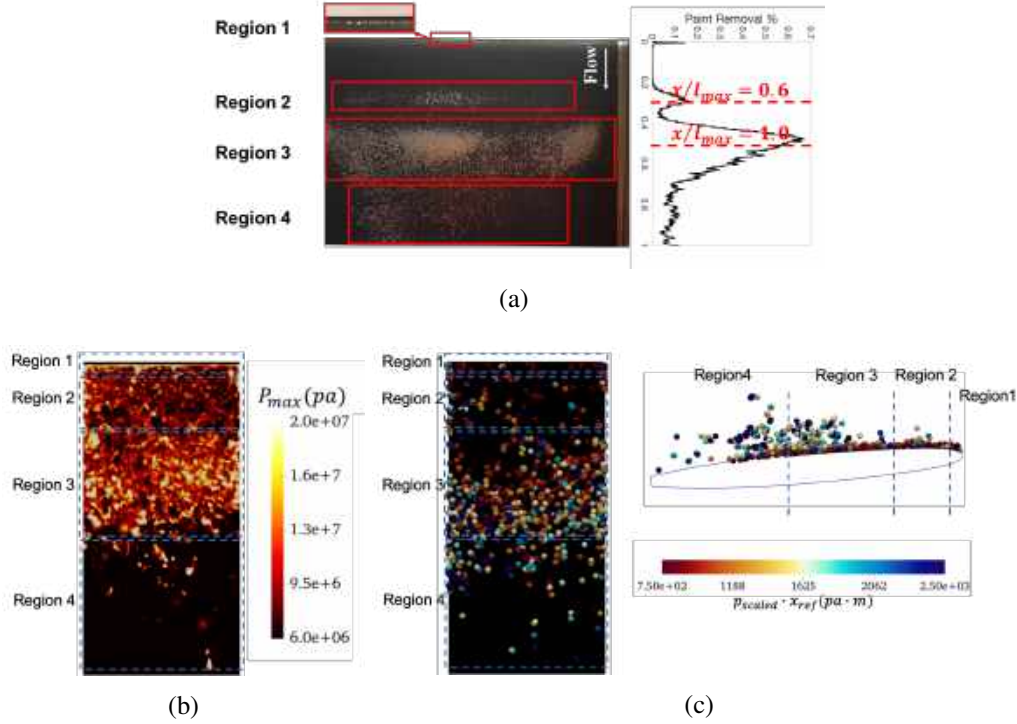


**Figure 4.5:** Location of aggressive collapses, a) Paint removal after 15 min of cavitation test ( $l_{max}$ : maximum length of the sheet cavity,  $x$ : stream-wise position from the leading edge), b) Maximum recorded pressure on each face element of the surface during over 10 shedding cycles in the compressible simulation, c) Spatial distribution of collapse points detected by incompressible simulation.

The above paint test and compressible simulation results showed that among the identified four regions, region 3 is associated with the highest risk of cavitation erosion. Figure 4.6 presents the hydrodynamic mechanisms of the three types of collapse events which are responsible for this high erosion risk in region 3. The first type is the collapse of small structures at the downstream end of the cloud. These structures are created due to the secondary shedding identified in Paper A. These small structures detach from the downstream end of the cloud and collapse shortly after their detachment, producing high pressure pulses on the surface in the simulation results according to Figure 4.6a. The second type of aggressive collapse events is the collapse of large vortical cavity structures in the cloud cavity, shown in Figure 4.6b. The structures are created when the small

structures in the upstream end of the cloud merge into a cavitating vortex. These cavitating vortices can undergo violent collapse due to the high pressure between the rolling cloud and growing sheet cavity. The reason for this high pressure (see Figure 4.1c) is explained in Paper A. The last detected type of aggressive collapse event in region 3 occurs in the vapor structures detached from the closure line of the sheet cavity. As shown in the summary of Paper A (see Figure 4.2), the closure line of the sheet cavity is unsteady due to its interaction with the re-entrant jet. The unsteady closure line releases vapor structures which collapse shortly after their detachment, possibly due to a high pressure in the closure line of the sheet cavity, and produce high-pressure pulses on the surface.

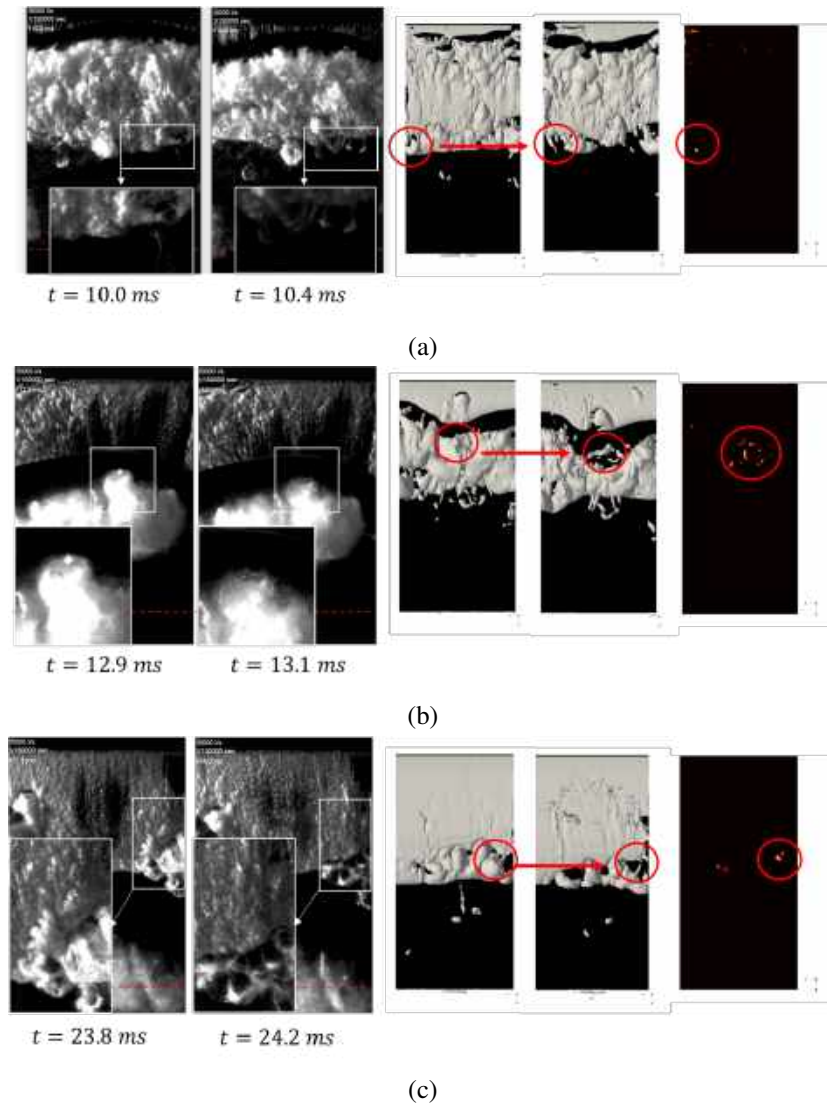


**Figure 4.6:** Collapse of cavity structures responsible for erosion pattern in region 3 (Flow is from top to bottom and the trailing edge is marked by a red dashed line).



### 4.3 PAPER C

In this paper, a new method to assess the risk of cavitation erosion using incompressible simulation of cavitating flows is presented. The method is based on the energy balance between the cavitating structures and cavitation erosion suggested by Hammitt [33]. In contrast to previous methods [29, 49, 35] in which the potential energy of collapsing cavities has been used for erosion assessment, the presented method uses the kinetic energy in the surrounding liquid to estimate the risk of cavitation erosion. By using this kinetic energy, the uncertainty related to the definition of collapse driving pressure in the potential energy formulation can be avoided. Furthermore, the developed method considers both shock-waves and micro-jets as the energy transfer mechanisms between the collapsing cavities and the surface material, while only one of these mechanisms was considered in published methods.

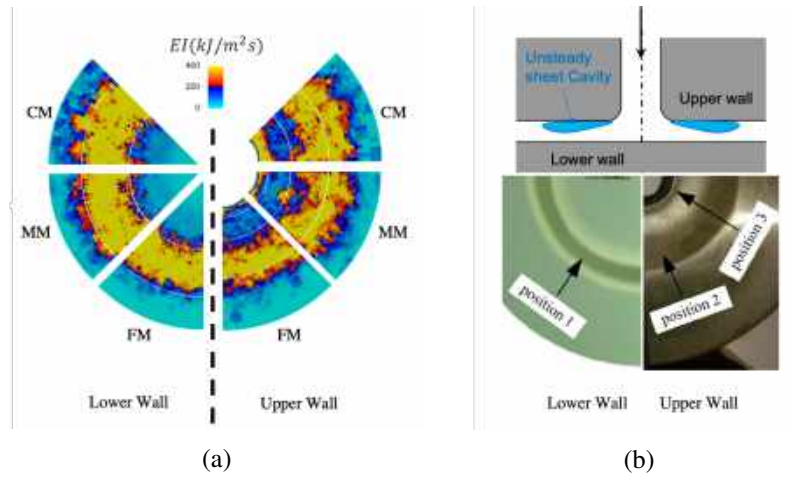


**Figure 4.7:** Numerical and the experimental erosion pattern, (a) the predicted areas with high risk of cavitation erosion in the simulation with different mesh resolution and (b) the erosion pattern in the experiment by Franc et al. [3].

In order to validate the method, the cavitating flow in a stagnation nozzle flow is simulated using three mesh resolutions, and the areas with predicted high risk of cavitation erosion are compared with the erosion pattern in the experiment by Franc et al. [3]. This comparison is presented in Figure 4.7. The experiment shows three main eroded regions, a region on the lower wall with the radial extension  $19\text{ mm} < r < 32\text{ mm}$ , a region on the upper wall with the radial extension  $17\text{ mm} < r < 27\text{ mm}$ , and a region on the upper wall between the pipe exit and  $r = 11\text{ mm}$ . These regions can be qualitatively predicted by the developed method in all three simulations with different mesh resolutions. Despite this qualitative agreement, the change in the mesh resolution slightly changes the radial extension of position 1 and 2 as well as the location of position 2. This mesh dependency for the position 3 is higher as the estimated erosion risk reduces progressively by increasing mesh

resolution. In Paper C, these mesh dependencies of the predicted erosion risk are investigated in detail and it is shown that they are due to slightly different cavitation dynamics captured in the simulations with different mesh resolutions.

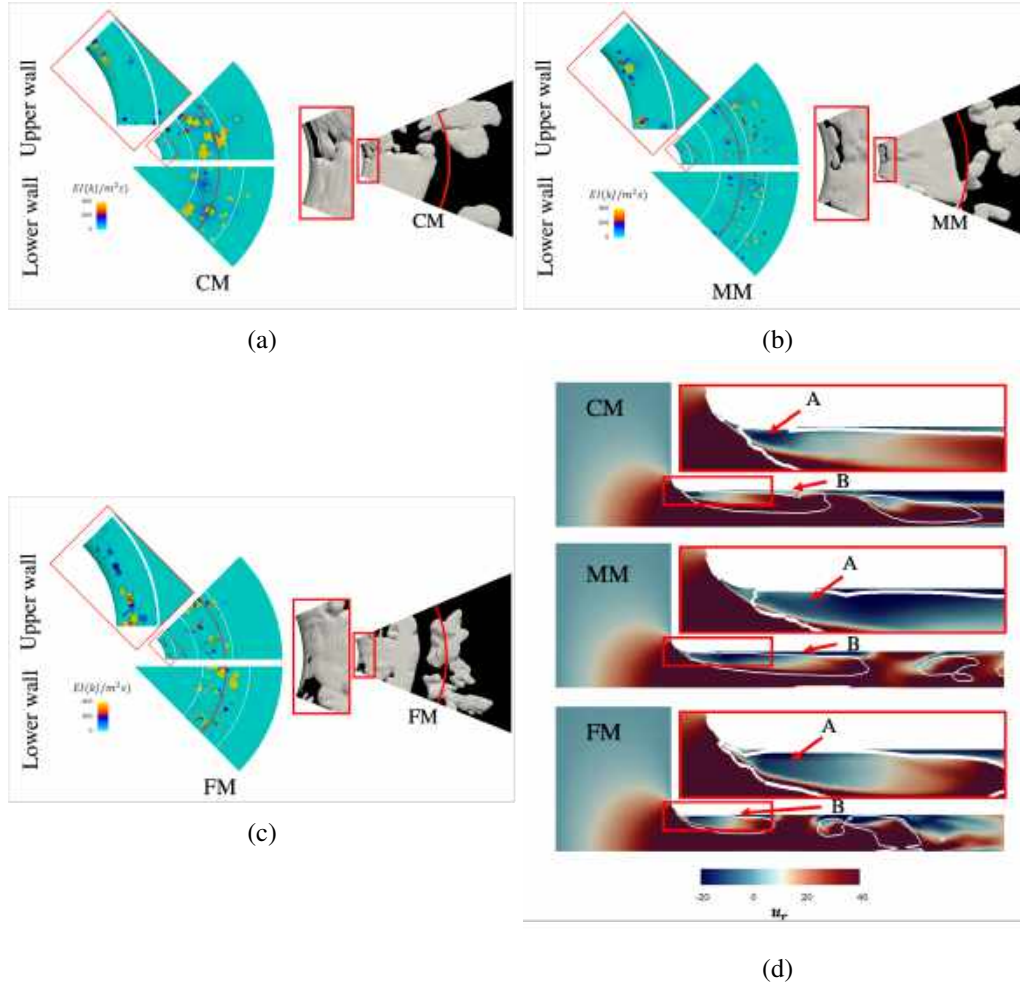


**Figure 4.8:** Presence of disturbance on the interface of the sheet cavity at its inception location and the estimated risk of cavitation erosion.

The hydrodynamic mechanisms responsible for the high risk of cavitation erosion at the inception region of the sheet cavity (position 3 in Figure 4.7) is discussed in Paper C in detail. A summary of this discussion is presented here. As it can be seen in Figures 4.8a, 4.8b, and 4.8c, the high risk of cavitation erosion in position 3 occurs mostly in the region where there is a disturbance in the interface of the sheet cavity near the pipe exit. At the location of these disturbances, the flow separates from the upper-wall due to the sharp turn as it is shown in Figure 4.8d. This separation zone (marked by A in Figure 4.8d) which has a high value of negative radial velocity, is connected to another reverse flow marked by B in Figure 4.8d. The interface of the sheet cavity (white lines in Figure 4.8d) indicates that the reverse flow marked by B originates from the closure line of the



sheet cavity and supplies packets of liquid at the downstream end of the separation zone. These liquid packets can go further upstream due to the reverse flow in the separation zone. If the upstream moving liquid packets have enough momentum to reach the pipe exit, they hit the flow exiting the pipe and this leads to a region of high pressure. This high pressure region can activate locally the condensation resulting in the disturbance at the interface of the sheet cavity and it can also trigger collapse events near the surface which are responsible for the high risk of cavitation erosion in position 3.

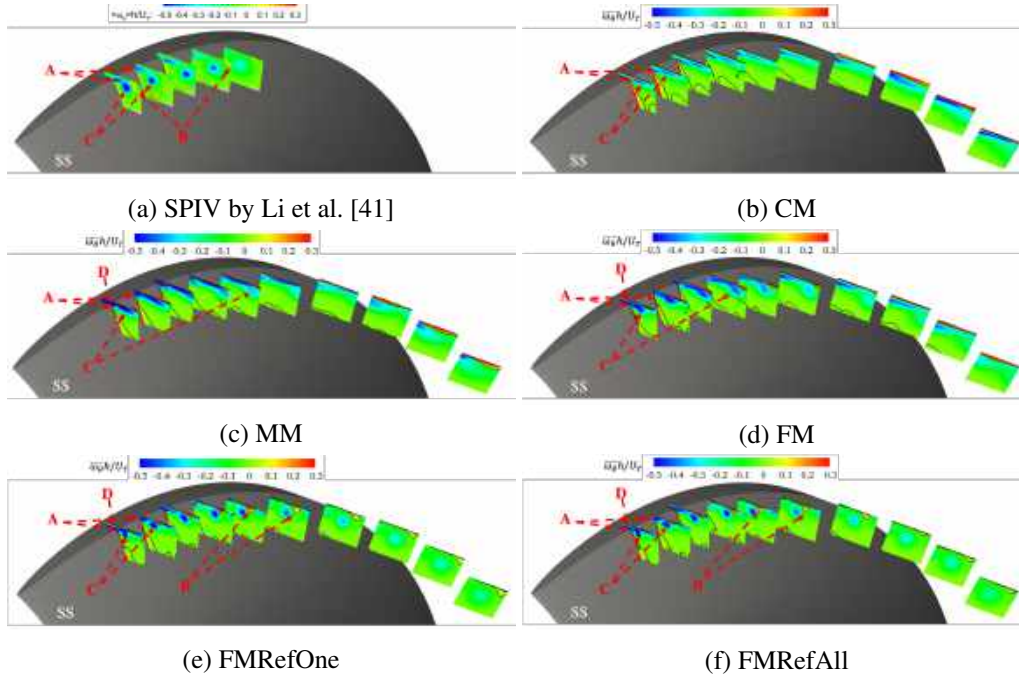


**Figure 4.9:** Comparison between the time averaged tangential vorticity field on different meridional planes in the experimental SPIV and numerical simulations obtained with different mesh resolutions ( The description of these mesh resolutions are presented in Table 3.5).

#### 4.4 PAPER D

In this paper, the non-cavitating and cavitating flows in the AxWJ-2 axial water-jet pump of Johns Hopkins University are simulated using a Large Eddy Simulation (LES) approach. The objective is to identify the mesh resolution needed to capture the main features of the flow in water-jet pumps. In order to find this mesh requirement, the simulation results obtained by different mesh resolutions are compared with the experimental data by Li et al. [41] and Tan et al. [14]. The description of these mesh resolutions are presented in Table 3.5. Figure 4.9 presents this comparison for the flow details near the blade tip. The experimental data by Li et al. [41] in Figure 4.9a shows that the flow details near the tip include three regions

with high vorticity generation. According to Wu et al. [10], these regions, denoted by A, B, and C in Figure 4.9a are, respectively, due to the shear layer between the reverse flow exiting the tip gap and the flow inside the passage, the boundary layer separation in the tip leakage flow near the rotor casing, and the core of Tip Leakage Vortex (TLV). In the simulation results obtained in the coarse mesh (Figure 4.9b), medium mesh (Figure 4.9c), and fine mesh (Figure 4.9d), the high vorticity due to the shear layer (region A) and the trace of the TLV core (region C) can be seen. However, the core of TLV is in the form of the sheet vortex rather than a cylindrical vortex as seen in the experiment and the mesh resolution near the shroud is too coarse to capture the boundary layer separation at the shroud. The results captured by the fine meshes with refinement at the tip (Figures 4.9e and 4.9f) shows that all three regions of the high vorticity are captured. Furthermore the core of the TLV has similar behavior as the one in the experiment. The main core of the TLV is connected to the shear layer in early stage of its development (closest plane to the leading edge in Figure 4.9), which indicates that the vortical structures in the shear layer are fed to the main core of TLV. Similar to the experiment, this feeding of the vortical structures stops when the TLV detached from the shear layer in the planes further downstream. The comparison between Figures 4.9e and 4.9f shows that almost the same TLV dynamics are captured in the results from the fine meshes with refined tip. This indicates that the interaction between the TLVs formed on the neighboring blades is insignificant, therefore refinement around one blade is enough for capturing the main flow feature in the leakage region.

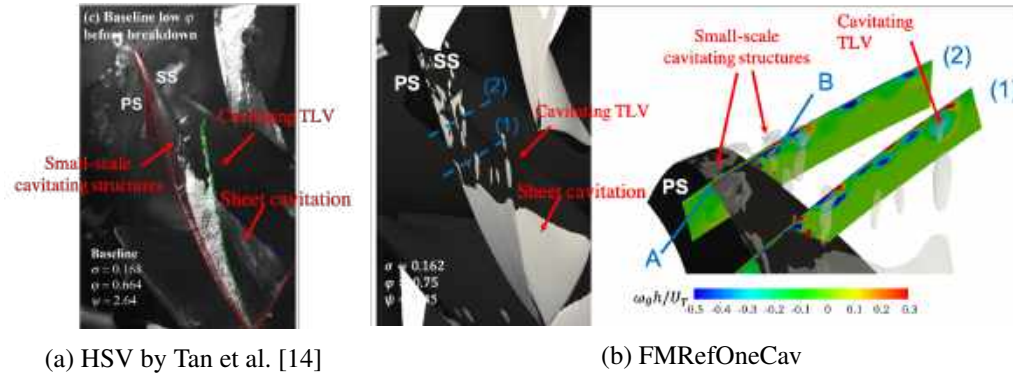


**Figure 4.10:** Comparison between cavitating regions in the numerical simulation and high speed visualization by Tan et al. [14].

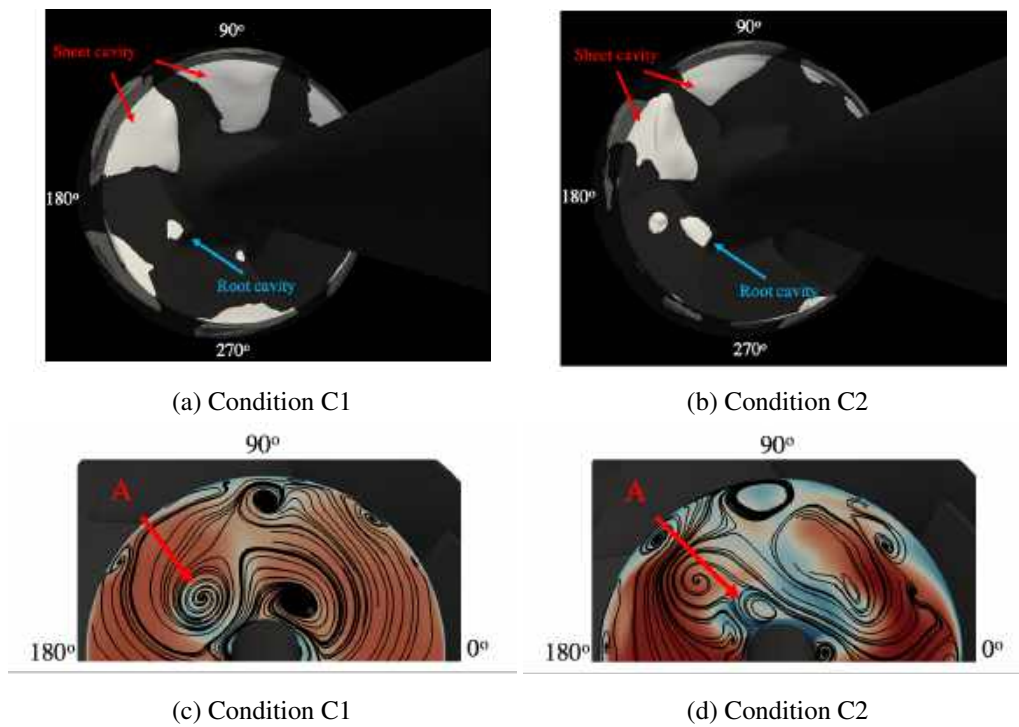
In Paper D, the comparison between the numerical simulations and the experimental data by Tan et al. [14] is made for the cavitating regions. This comparison is shown in Figure 4.10. Note that the mesh resolution in the simulation results in this figure is the same as the one in Figure 4.9e and that this mesh resolution is shown to capture the flow detail in the experiment. In the experiment, three main cavitating structures are present which are (1) the sheet cavitation formed on the suction side of the blade, (2) the large-scale cavitating TLV, (3) the small-scale

cavitating structures formed downstream of the cavitating TLV. The numerical results show that the same three cavitating regions can be captured by the numerical simulation. In order to investigate the origin of small-scale cavitating structures after TLV, zoom-in view of these structures is shown in Figure 4.10b. The figure also includes the tangential vorticity distribution on two planes. These distribution indicates that two regions with a high value of tangential vorticity are responsible for the formation of these small-scale structures. These regions are the separation zone at the edge of blade on the pressure side (A in the close-up view) and the shear layer attached to the suction side of the blade (B in the close-up view).

## 4.5 PAPER E

In this paper, the risk of cavitation erosion is assessed in a commercial mixed-flow water-jet pump using the numerical erosion assessment method presented in Paper C. This assessment is performed for two operating conditions which have different risk of cavitation erosion. The investigations of these conditions are performed in two steps. First, the hydrodynamics mechanisms responsible for the formation of different cavitating structures are investigated using a detail analysis of numerical results. Secondly, the risk of cavitation erosion assessed using the numerical method in Paper C are compared with the experimental paint test performed for the conditions similar to the simulations and the relation between the cavitation dynamics and areas with high risk of cavitation erosion are investigated for the most erosive flow condition.

Figures 4.11a and 4.11b show the cavitation dynamics in two studied conditions in the simulation results. It can be seen that a sheet cavity forms at the leading-edge of the blade when it passes the position of  $90^\circ$ . This sheet cavity grows up to the position of  $180^\circ$  and then starts to shrink. At the position of  $225^\circ$ , the sheet cavity almost completely disappears except for the root cavity which is marked in the figures. This root cavity which is quite larger in condition C2, disappears as the blade rotates further. In order to explain the origin of the cavitation dynamics in the two studied conditions, the distribution of axial velocity on a plane in the intake duct is shown in Figures 4.11c and 4.11d. These distributions show that regions of low axial velocity are present in the upper part of the flow entering the rotor. As the blade passes through these low velocity regions, the inflow angle of attack relative to the blade increases. This higher angle of attack creates low pressure regions near the blade where different cavitating structures can incept. The figures also show that a low axial velocity region, marked by A, exists near the shaft. In Paper E, it is shown that this low axial velocity region is created due to the spiral form of vortex breakdown in the vortex shed from the shaft. The comparison between the two conditions shows that this region is larger in the condition C2. As this low axial velocity region is responsible for the formation of the root cavity, this cavity is larger in condition C2 as shown in Figures 4.11a and 4.11b.



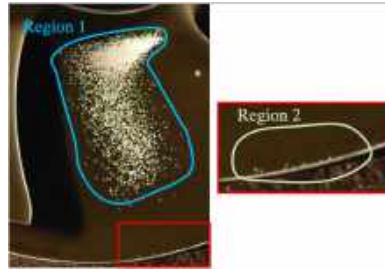
**Figure 4.11:** Cavitation dynamics and the inflow axial velocity entering the rotor, a and b) the cavitation dynamics in the simulations for two conditions, c and d) the axial velocity and in-plane streamlines on a plane in the intake duct.

Figure 4.12 presents the risk of cavitation erosion obtained by the paint test and the numerical method presented in Paper C for the two studied conditions. It can be seen in the paint test results that the risk of cavitation erosion is lower in condition C1 compared to condition C2. This trend can be captured in the numerical results which indicates the presented method can be used to rank the erosiveness of flow conditions in water-jet pumps. The experimental paint test also shows that the risk of cavitation erosion in conditions C1 and C2 occurs mostly near the root and the middle of the blade. Similar region of high erosion risk can be seen in the numerical simulation which is marked by region 1 in Figures 4.12c and 4.12d. It can also be seen that the numerical method predicts a region of high erosion risk near the tip of the blade (region 2 in Figure 4.12c and 4.12d) for both conditions. In condition C1, this region is not present in the paint test while for condition C2, the risk in this region is over-predicted compared to the paint test. In Paper E, it is argued that this difference is due to a slightly over-prediction of cavitating structures near the tip of the blade in the simulations, a high uncertainty in the paint test results near the tip of the blade and a different level of capturing small-scale cavitating structures in the tip regions compared to the other parts of the blade.

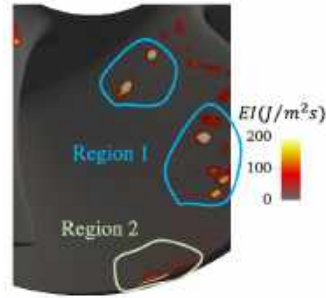
In Paper E, the hydrodynamic mechanisms responsible for the risk of cavi-



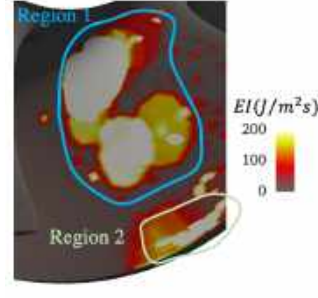
(a) Paint test for condition C1



(b) Paint test for condition C2



(c) Numerical results for condition C1



(d) Numerical results for condition C2

**Figure 4.12:** Risk of cavitation erosion obtained by the experimental paint test and presented numerical method in different flow conditions.

tation erosion in the condition C2 (Figures 4.12b and 4.12d) are investigated in detail. Figure 4.13 shows these mechanisms for region 1 in Figures 4.12b and 4.12d. It can be seen that the high erosion risk in this region is mostly due to the collapse events around the closure line of the sheet cavity (marked by A) and root cavity (marked by B). These collapse events occur when the blade leaves the low velocity region A shown in Figure 4.11d which leads to a decrease in the inflow angle of attack relative to the blade. This decrease in relative angle of attack then results in an increase in the pressure around the blade which triggers the collapse events shown in Figure 4.13.

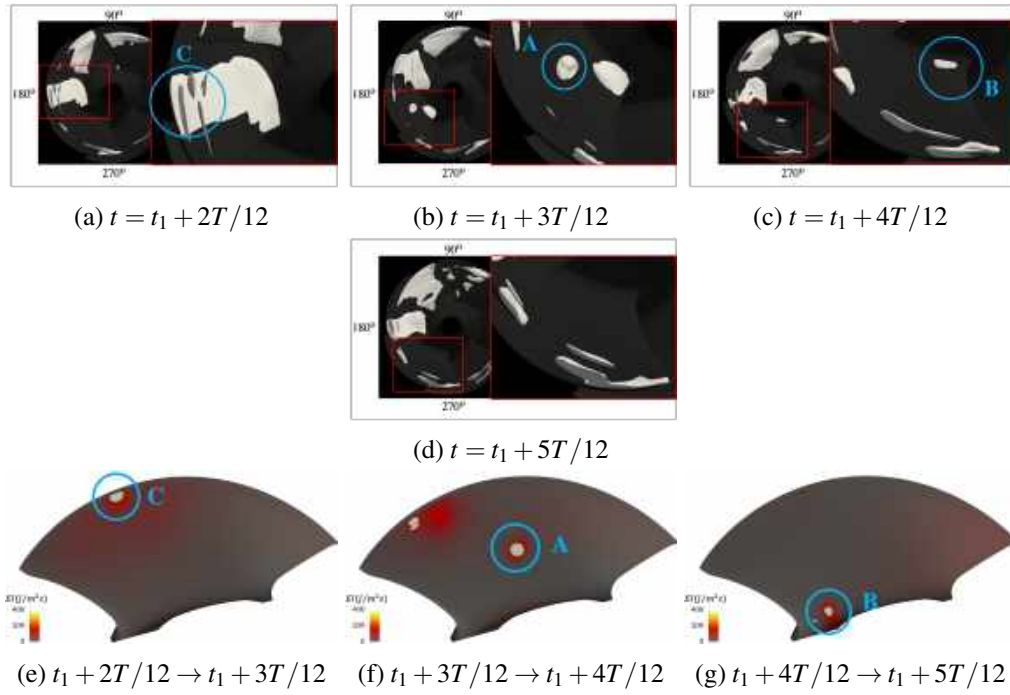


**Figure 4.13:** Relation between the cavitation dynamics and the risk of cavitation erosion, a-d) cavitation dynamics shown by the iso-surface of  $\alpha^l = 0.9$ , e-g) estimated risk of cavitation erosion between the interval of cavitation dynamics shown in a-d.

---

# 5

## *Concluding remarks*

---

This thesis concerns the development and application of numerical methods which are capable of assessing the risk of cavitation erosion. These numerical methods are highly desired from the industrial point of view as they can complement the shortcomings of experimental erosion assessment. Two numerical erosion assessment methods are considered in this thesis and both are implemented in the OpenFOAM framework. The first numerical erosion assessment method, which has been developed in this thesis, is based on incompressible simulation of cavitating flows while the second method, originally developed by Schnerr et al. [1], can assess the risk of cavitation erosion based on compressible simulations of cavitating flows. The risk of cavitation erosion predicted by these two methods are compared with the experimental study by Franc et al. [3] and the experimental paint results presented in this thesis. This comparison shows that the areas with a high erosion risk predicted by both methods match qualitatively well with the experimental results.

The above mentioned numerical erosion assessment methods are applied to two cavitating flows, the leading-edge cavitation formed over a 3D NACA0009 wing and the cavitating flow in an axisymmetric nozzle. The main objective in this part is to identify hydrodynamic mechanisms in erosive cavitation. For the leading-edge cavitation, it can be concluded that these hydrodynamic mechanisms are mostly governed by two distinctive shedding mechanisms of transient cavities, primary shedding and secondary shedding. The primary shedding produces large-scale cloud cavities in a periodic manner, while the secondary shedding results in the formation of small-scale cloud cavities from the closure line of the sheet cavity and downstream end of the large-scale cloud cavity. It is also observed that although the transient cavities due to both shedding mechanisms are associated with risk of cavitation erosion, the small scale cavity structures in secondary shedding possess higher risk of cavitation erosion as they leads to a larger number of aggressive collapse events which occur closer to the surface. This finding

highlights the necessity of capturing the secondary shedding in the numerical simulations with the aim of assessing the risk of cavitation erosion. For the cavitating flow in the axisymmetric nozzle, the hydrodynamic mechanisms responsible for the risk of cavitation erosion at the inception region of the sheet cavity are investigated. It is shown that this risk is related to the separation zone present in this region. This separation zone augments the reverse liquid flow which is present underneath the sheet cavity. The augmented liquid flow can then travel upstream and hit the inflow near the inception region. This collision increases the pressure locally which can trigger aggressive collapse events with high risk of cavitation erosion.

The last part of this thesis is devoted to the numerical simulation of cavitating flows in water-jet pumps. The main objective of this part is to apply the developed numerical erosion assessment method to a commercial water-jet pump. As the first step toward this objective, the mesh resolution requirement for high quality water-jet pump simulations is identified. It is shown that the flow details in water-jet pumps can be captured if a mesh refinement region with at least 40 cells in the tip gap is applied around the blade tip that the mesh refinement can be applied on only one blade as there is a weak interaction between flow of the neighboring blades. Using the identified mesh requirement in the first step, a commercial mixed-flow water-jet pump is simulated and the risk of cavitation erosion is assessed numerically for two flow conditions. These conditions are associated with different risk of cavitation erosion according to the experimental paint test performed at Kongsberg Hydrodynamic Research Centre (KHRC). The comparison between this paint test and numerical results shows that the developed numerical erosion assessment method is able to capture the difference between the risk of cavitation in two studied conditions. It is also shown that the developed method can identify areas with high risk of cavitation erosion which are present in the experimental paint test. From the detail analysis of numerical simulations, it can be concluded that the high risk in these areas is due to collapse of the root cavity and the sheet cavity near the root of the rotor blade. The simulation results also show that these cavities are formed when the blade enters the low axial velocity regions present in the inflow. As the blade leaves these regions, the pressure around the blade recovers which leads to aggressive collapse events in the root and sheet cavities.



---

## REFERENCES

---

- [1] G.H. Schnerr, I.H. Sezal, and S.J. Schmidt. Numerical investigation of three-dimensional cloud cavitation with special emphasis on collapse induced shock dynamics. *Physics of Fluids*, 20(4):040703, 2008.
- [2] M. Mihatsch, S. Schmidt, and N. Adams. Cavitation erosion prediction based on analysis of flow dynamics and impact load spectra. *Physics of Fluids*, 27(10):103302, 2015.
- [3] J. Franc, M. Riondet, A. Karimi, and G.L. Chahine. Impact load measurements in an erosive cavitating flow. *Journal of Fluids Engineering*, 133(12):121301, 2011.
- [4] T. Pham, F. Larrarte, and D. Fruman. Investigation of unsteady sheet cavitation and cloud cavitation mechanisms. *Journal of Fluids Engineering*, 121(2):289–296, 1999.
- [5] Y. Kawanami, H. Kato, H. Yamaguchi, M. Tanimura, and Y. Tagaya. Mechanism and control of cloud cavitation. *Journal of Fluids Engineering*, 119(4):788–794, 1997.
- [6] B. Budich, S. Schmidt, and N. Adams. Numerical simulation and analysis of condensation shocks in cavitating flow. *Journal of Fluid Mechanics*, 838:759–813, 2018.
- [7] H. Ganesh, S. A Mäkiharju, and S. Ceccio. Bubbly shock propagation as a mechanism for sheet-to-cloud transition of partial cavities. *Journal of Fluid Mechanics*, 802:37–78, 2016.
- [8] J.K. Jakobsen. On the mechanism of head breakdown in cavitating inducers. *Journal of Basic Engineering*, 86(2):291–305, 1964.
- [9] R.L. Miorini, H. Wu, and J. Katz. The internal structure of the tip leakage vortex within the rotor of an axial waterjet pump. *Journal of Turbomachinery*, 134(3):031018, 2012.

- [10] H. Wu, R. L. Miorini, D. Tan, and J. Katz. Turbulence within the tip-leakage vortex of an axial waterjet pump. *AIAA Journal*, 50(11):2574–2587, 2012.
- [11] D. Tan, R. Miorini, J. Keller, and J. Katz. Flow visualization using cavitation within blade passage of an axial waterjet pump rotor. In *ASME 2012 Fluids Engineering Division Summer Meeting collocated with the ASME 2012 Heat Transfer Summer Conference and the ASME 2012 10th International Conference on Nanochannels, Microchannels, and Minichannels*, pages 395–404. American Society of Mechanical Engineers, 2012.
- [12] R. Laborde, P. Chantrel, and M. Mory. Tip clearance and tip vortex cavitation in an axial flow pump. *Journal of Fluids Engineering*, 119(3):680–685, 1997.
- [13] F. Avellan. Introduction to cavitation in hydraulic machinery. In *The 6th International Conference on Hydraulic Machinery and Hydrodynamics, Timisoara, Romania*, pages 21–22, 2004.
- [14] D. Tan, Y. Li, I. Wilkes, E. Vagnoni, R. Miorini, and J. Katz. Experimental investigation of the role of large scale cavitating vortical structures in performance breakdown of an axial waterjet pump. *Journal of Fluids Engineering*, 137(11):111301, 2015.
- [15] S. Fujikawa and T. Akamatsu. Effects of the non-equilibrium condensation of vapour on the pressure wave produced by the collapse of a bubble in a liquid. *Journal of Fluid Mechanics*, 97(3):481–512, 1980.
- [16] E. Johnsen and T. Colonius. Numerical simulations of non-spherical bubble collapse. *Journal of Fluid Mechanics*, 629:231–262, 2009.
- [17] H. Lee, A. Gojani, T. Han, and J. Yoh. Dynamics of laser-induced bubble collapse visualized by time-resolved optical shadowgraph. *Journal of Visualization*, 14(4):331–337, 2011.
- [18] M. Plesset and R.B. Chapman. Collapse of an initially spherical vapour cavity in the neighbourhood of a solid boundary. *Journal of Fluid Mechanics*, 47(2):283–290, 1971.
- [19] G. Bark, N. Berchiche, and M. Grekula. Application of principles for observation and analysis of eroding cavitation-the erocav observation handbook. *EROCav Report, Dept. of Naval Architecture, Chalmers University of Technology, Göteborg, Sweden*, 2004.
- [20] M. Van Rijsbergen, E. Foeth, P. Fitzsimmons, and A. Boorsma. High-speed video observations and acoustic-Impact measurements on a NACA0015 foil. In *Proceedings of the 8th International Symposium on Cavitation, Singapore*, 2012.
- [21] W. Pfitsch, S. Gowing, D. Fry, M. Donnelly, and S. Jessup. Development of measurement techniques for studying propeller erosion damage in severe wake fields. In *7th International Symposium on Cavitation, Michigan, USA*, 2009.

- 
- [22] Y. Cao, X. Peng, K. Yan, L. Xu, and L. Shu. A qualitative study on the relationship between cavitation structure and erosion region around a 3d twisted hydrofoil by painting method. In *Fifth International Symposium on Marine Propulsors, Finland*, 2017.
- [23] P. Koukouvini, N. Mitroglou, M. Gavaises, M. Lorenzi, and M. Santini. Quantitative predictions of cavitation presence and erosion-prone locations in a high-pressure cavitation test rig. *Journal of Fluid Mechanics*, 819:21–57, 2017.
- [24] C. Egerer, S. Hickel, S. Schmidt, and N. Adams. Large-eddy simulation of turbulent cavitating flow in a micro channel. *Physics of Fluids*, 26(8):085102, 2014.
- [25] F. Örley, S. Hickel, S.J. Schmidt, and N.A. Adams. Large-eddy simulation of turbulent, cavitating fuel flow inside a 9-hole diesel injector including needle movement. *International Journal of Engine Research*, 18(3):195–211, 2017.
- [26] B. Budich, S. Schmidt, and N. Adams. Numerical investigation of a cavitating model propeller including compressible shock wave dynamics. In *Fourth International Symposium on Marine Propulsors, Texas, USA*, 2015.
- [27] B. Budich, S. Schmidt, and N. Adams. Numerical simulation of cavitating ship propeller flow and assessment of erosion aggressiveness. In *Fourth International Symposium on Marine Propulsors, Texas, USA*, 2015.
- [28] N. Ochiai, Y. Iga, M. Nohmi, and T. Ikohagi. Study of quantitative numerical prediction of cavitation erosion in cavitating flow. *Journal of Fluids Engineering*, 135(1):011302, 2013.
- [29] R. Fortes-Patella, J. Reboud, and L. Briancon-Marjollet. A phenomenological and numerical model for scaling the flow aggressiveness in cavitation erosion. In *ERO-CAV Workshop, Val de Reuil, France*, volume 11, pages 283–290, 2004.
- [30] M. Dular, R. Bachert, B. Stoffel, and B. Širok. Experimental evaluation of numerical simulation of cavitating flow around hydrofoil. *European Journal of Mechanics-B/Fluids*, 24(4):522–538, 2005.
- [31] A. Peters, H. Sagar, U. Lantermann, and O. el Moctar. Numerical modelling and prediction of cavitation erosion. *Wear*, 338:189–201, 2015.
- [32] T. Van, P. Fitzsimmons, E. Foeth, and Z. Li. Cavitation erosion: A critical review of physical mechanisms and erosion risk models. In *7th International Symposium on Cavitation, Michigan, USA*, 2009.
- [33] F. G. Hammit. Observations on Cavitation Damage in a Flowing System. *Journal of Fluids Engineering*, 85(3):347–356, 09 1963. ISSN 0098-2202.
- [34] S. Schenke, T. Melissaris, and T. van Terwisga. On the relevance of kinematics for cavitation implosion loads. *Physics of Fluids*, 31(5):052102, 2019.
-

- [35] T. Melissaris, N. Bulten, and T. van Terwisga. On the applicability of cavitation erosion risk models with a urans solver. *Journal of Fluids Engineering*, 141(10): 101104, 2019.
- [36] R. Fortes-Patella, A. Archer, and C. Flageul. Numerical and experimental investigations on cavitation erosion. In *IOP Conference Series: Earth and Environmental Science*, volume 15, page 022013. IOP Publishing, 2012.
- [37] T. Huuva. *Large eddy simulation of cavitating and non-cavitating flow*. PhD thesis, Chalmers University of Technology, 2008.
- [38] N. Lu, R.E. Bensow, and G. Bark. Large eddy simulation of cavitation development on highly skewed propellers. *Journal of Marine Science and Technology*, 19(2): 197–214, 2014.
- [39] A. Asnaghi, A. Feymark and R.E. Bensow. Numerical investigation of the impact of computational resolution on shedding cavity structures. *International Journal of Multiphase Flow*, 2018.
- [40] T. Michael, S. Schroeder, and A. Becnel. Design of the ONR AxWJ-2 axial flow water jet pump. Technical report, Hydromechanics Department Report No. NSWCCD-50TR-2008/066., 2008.
- [41] Y. Li, D. Tan, H. Chen, and J. Katz. Stereoscopic piv measurement of the flow in the tip region of an axial waterjet pump. In *16th International Symposium on Transport Phenomena and Dynamics of Rotating Machinery*, 2016.
- [42] R.E. Bensow and G. Bark. Implicit LES predictions of the cavitating flow on a propeller. *Journal of Fluids Engineering*, 132(4):041302, 2010.
- [43] N. Lu, R. E. Bensow, and G. Bark. LES of unsteady cavitation on the delft twisted foil. *Journal of Hydrodynamics, Ser. B*, 22(5):784–791, 2010.
- [44] A. Asnaghi, A. Feymark and R.E. Bensow. Improvement of cavitation mass transfer modeling based on local flow properties. *International Journal of Multiphase Flow*, 93:142–157, 2017.
- [45] F. Nicoud and F. Ducros. Subgrid-scale stress modelling based on the square of the velocity gradient tensor. *Flow, turbulence and Combustion*, 62(3):183–200, 1999.
- [46] J. Sauer. Instationär kavitierende strömungen-ein neues modell, basierend auf front capturing (vof) und blasendynamik. *Diss., Uni Karlsruhe*, 2000.
- [47] L. Yuan-Hui. Equation of state of water and sea water. *Journal of Geophysical Research*, 72(10):2665–2678.
- [48] S.J. Schmidt, M.S. Mihatsch, M. Thalhamer, and N.A. Adams. Assessment of erosion sensitive areas via compressible simulation of unsteady cavitating flows. In *Advanced experimental and numerical techniques for cavitation erosion prediction*, pages 329–344. Springer, 2014.

- [49] S. Schenke and T. van Terwisga. An energy conservative method to predict the erosive aggressiveness of collapsing cavitating structures and cavitating flows from numerical simulations. *International Journal of Multiphase Flow*, 111:200–218, 2019.
- [50] T. Okada, Y. Iwai, S. Hattori, and N. Tanimura. Relation between impact load and the damage produced by cavitation bubble collapse. *Wear*, 184(2):231–239, 1995.
- [51] R. Fortes-Patella, G. Challier, J. Reboud, and A. Archer. Energy balance in cavitation erosion: from bubble collapse to indentation of material surface. *Journal of Fluids Engineering*, 135(1):011303, 2013.
- [52] M. Gavaises, F. Villa, P. Koukouvini, M. Marengo, and J. Franc. Visualisation and LES simulation of cavitation cloud formation and collapse in an axisymmetric geometry. *International Journal of Multiphase Flow*, 68:14–26, 2015.

## REFERENCES

---

---

# **APPENDIX A**

## **Appended Papers A-E**

